

Imaging of Adult Ocular and Orbital Pathology - a Pictorial Review

Reuben Grech^{1*}, Kurt Spiteri Cornish², Patrick Leo Galvin¹, Stephan Grech³, Seamus Looby¹, Alan O'Hare¹, Adrian Mizzi³, John Thornton¹, Paul Brennan¹

1. Department of Neuroradiology, Beaumont Hospital, Dublin, Republic of Ireland

2. Department of Ophthalmology, Aberdeen Royal Infirmary, Foresterhill, United Kingdom

3. Department of Radiology, Mater Dei Hospital, Malta

* **Correspondence:** Reuben Grech, Department of Neuroradiology, Beaumont Hospital, Beaumont Road Dublin 9, Republic of Ireland
(✉ reubengrech@yahoo.com)

Radiology Case. 2014 Feb; 8(2):1-29 :: DOI: 10.3941/jrcr.v8i2.1525

ABSTRACT

Orbital pathology often presents a diagnostic challenge to the reporting radiologist. The aetiology is protean, and clinical input is therefore often necessary to narrow the differential diagnosis. With this manuscript, we provide a pictorial review of adult ocular and orbital pathology.

PICTORIAL REVIEW

PICTORIAL REVIEW

INTRODUCTION

The anatomical compartment involved by the pathological process together with the presence of pathognomonic imaging findings can often guide the radiological interpretation. In this pictorial review we classify ocular and orbital pathology in major etiological categories whilst attempting to highlight the characteristic imaging findings.

ANATOMY

The orbit is 'the cavity in the skull of a vertebrate that contains the eye; the eye socket'[1]. The volume of the adult human orbit is about 30cc, of which the eye occupies just 6.5cc[2]. The orbits are conical or four-sided pyramidal structures.

Seven facial bones namely the frontal, zygomatic, lacrimal, sphenoid, palatine, ethmoid and maxillary bones form the bony contours.

The optic foramen which leads to the optic canal lies at the nasal end of the superior orbital fissure. The optic canal

leads to the middle cranial fossa and transmits the optic nerve and the ophthalmic artery. The superior orbital fissure lies between the lesser and greater wings of the sphenoid bone and transmits the ophthalmic nerve (Va), ophthalmic veins, oculomotor nerve (III), trochlear nerve (IV), abducent nerve (VI), sympathetic fibers and branches of the meningeal and lacrimal arteries[3]. The inferior orbital fissure lies where the floor meets the lateral wall of the orbit and connects the orbit to the pterygopalatine and infra-temporal fossae. Structures passing through the fissure include the infra-orbital and zygomatic branches of the maxillary nerve (Vb), the inferior ophthalmic vein and the orbital branches of the pterygopalatine ganglion. Medially one finds the groove for the nasolacrimal duct, which connects the lacrimal sac to the nasolacrimal opening in the inferior nasal meatus.

The soft tissue complex of the orbit is divided into five main groups; the orbital septum, the periorbital fat, the extra-ocular muscles and the lacrimal system. The orbital septum has a mesodermal origin and is covered anteriorly by pre-septal orbicularis muscle. It is a thin structure formed by multi-layered fibrous tissue. The periorbital fat is essentially the periosteal lining of orbital walls, and is attached to the orbital fissures and foramina. The six extra ocular muscles arise from the annulus of Zinn and are responsible for the movements of

the globe. The lacrimal gland lies in the shallow lacrimal fossa of the frontal bone at the supero-temporal portion of the orbit.

The orbital septum (also known as the palpebral ligament) represents a fibrous septum which extends from the bony margins of the orbital rim and blends with the tendon of levator palpebrae superioris and the tarsal plate in the upper and lower eyelids respectively. It also forms an important clinical boundary particularly in cases of orbital cellulitis. Involvement of the orbital structures anterior to the septum is referred to as peri-orbital cellulitis as opposed to orbital cellulitis where infection crosses the septum.

The extra-ocular muscles are arranged in a cone converging towards the optic canal. They divide the retro-orbital space into intra- and extra- conal spaces referring to the space within the muscles and external to the muscles respectively. Hence the space within the orbit can be divided into 4 spaces namely the ocular, intra-conal, conal and extra-conal spaces - such characterization is essential to narrow the differential diagnosis of ocular diseases.

VASCULAR

Vascular lesions account for 5-20% of orbital masses[4]. Much controversy exists regarding the nomenclature and classification of these lesions. The Orbital Society proposed a classification scheme based on hemodynamic flow within the lesion[5]. Another classification which takes account of the natural history, the growth pattern and histological features was proposed by Mulliken and Glowacki[6]. It classifies vascular lesions into the following groups: capillary haemangiomas, venous vascular malformations (cavernous malformations and orbital varices), venous lymphatic malformations (capillary, cavernous, and cystic lymphatic malformations), arterial and arterio-venous lesions (arterio-venous malformations, arterio-venous fistulas, and ophthalmic artery aneurysms), neoplasms (haemangioblastomas, haemangiopericytomas, choroidal haemangiomas, choroidal melanomas and vascular metastases), and miscellaneous (Coats disease)[7].

Capillary hemangioma (figure 1) is the most common orbital vascular tumour of infancy, and has no known familial or hereditary association. There is a female predilection with a male-to-female ratio of 2:3[8]. Lesions may either present at birth or appear shortly after, and rapidly increase in size during the first year of life. A short period of stabilization follows and then lesion involution which may last up to 10 years is expected[6]. Most are extra-conal in location but they tend to cross tissue planes and may even extend intra-cranially through the optic canal or the superior orbital fissure[9]. Occasionally haemangiomas may involve the extra-ocular muscles and lacrimal glands[10]. Radiologic evaluation is required for diagnosis and therapy planning. Since haemangiomas lack a capsule they appear as lobulated, irregularly marginated masses on CT. Intra-lesional calcifications are rare. In the proliferative phase haemangiomas are typically homogeneous and isodense to muscle. Intense, persistent and homogenous enhancement is appreciated after contrast administration. The lesion becomes

more heterogeneous during the involution phase, and contrast enhancement is markedly reduced[11,12]. Capillary haemangiomas demonstrate isointensity to muscle on T1W-images, and are moderately hyperintense on T2W-images. Similar enhancement characteristics as displayed on CT are also demonstrated in MRI. Lobules with thin dark fibrous septa, together with flow voids at the periphery of or within the tumour itself are considered characteristic imaging features[9]. Lesion vascularity and prominent feeding vessels are clearly depicted using MRA[11]. Conventional angiography is nowadays only performed when endovascular treatment is contemplated.

An orbital varix (figure 2) represents a distensible low-flow dilated vein or group of veins. The veins often maintain direct continuity with the systemic circulation and hence engorge whenever intracranial pressure rises. Imaging demonstrates tortuous tubular channels which taper towards the orbital apex and characteristically lack internal septations. Increase in size following Valsalva maneuver or jugular compression is considered pathognomonic[13]. Calcified phleboliths are also characteristic. Varices may appear inherently hyperdense on CT, and enhance profusely with contrast. The presence of prominent flow voids in MRI and tortuous anechoic tubular channels with low-velocity Doppler flow on US favor the diagnosis. Intracranial venous malformations are present in up to 10% of cases[14], thus brain imaging is mandatory.

Intracranial arterio-venous malformations (figure 3) may extend directly into the orbit or merely cause secondary engorgement of the ophthalmic veins from the increased venous pressure and congestion of the draining veins[15].

Orbital varices may also be secondary to carotico-cavernous fistulae (figure 4) due to direct arterio-venous shunting. Carotico-cavernous fistulae (CCFs) may either occur spontaneously or follow trauma. Imaging characteristically demonstrates a distended ipsilateral superior ophthalmic vein and engorgement of the ipsilateral cavernous sinus[16]. Conventional angiography is still considered the gold standard investigation whilst offering the possibility of endovascular treatment. Treatment varies according to the etiology and velocity of flow across the fistula[17].

INFLAMMATORY & INFECTIOUS

Orbital infections (figure 5) are often classified as pre-septal, post-septal and sub-periosteal according to the compartment which is primarily affected[18]. The infectious process can however spread to involve adjacent compartments. Radiologically, diffuse soft tissue swelling, orbital fat stranding and small pockets of gas characterize this condition. Abscess formation is seen as a rim enhancing fluid collection, and the presence of an air-fluid level is considered pathognomonic[19]. The primary imaging role is to evaluate spread of infection and assess for development of complications, which include intracranial sequelae.

Less commonly, infection may involve the ocular compartment via a hematogenous route. Ocular tuberculoma

(figure 6) often affects the choroid and retinal detachment may complicate the infection due to abundant exudate formation. The tuberculoma itself may mimic ocular lymphoma and choroidal melanoma[20], thus correlation with the patient's clinical history is imperative.

Orbital pseudotumour (figure 7) often presents with unilateral painful exophthalmos. Pathologically it is a non-granulomatous inflammatory disorder of unknown etiology. Imaging features are protean, and often non-specific. The radiological appearance may mimic several orbital disorders and pseudotumour remains a diagnosis of exclusion[21]. Not uncommonly, it presents as an infiltrative mass which may either involve the orbit diffusely or else demonstrate differential involvement of anatomical structures including the extra-ocular muscles, the lacrimal glands or the retro-orbital fat. Contrast enhancement is variable. MRI shows higher specificity than CT and may demonstrate typical low T1- and T2- signal intensity in keeping with the fibrous nature of the condition[22].

Optic neuritis (figure 8) has a multitude of causes[23] with multiple sclerosis being the commonest of these. Visual dysfunction is the presenting symptom in a third of cases, and ocular involvement occurs in up to 75% of patients throughout the course of the illness[24]. In the acute stage MR demonstrates diffuse swelling of the optic nerve with focal plaques of T2 hyperintensity[13]. Fat saturation techniques annul the high signal of the adjacent orbital fat resulting in improved sensitivity. Contrast enhancement is occasionally appreciated. Review of the entire scan may reveal additional areas of demyelination which further support the diagnosis.

ENDOCRINE

Although secondary involvement of the orbits can be attributed to a whole spectrum of endocrine disturbances, thyroid eye disease is by far the commonest culprit.

Thyroid orbitopathy (figure 9) often presents in middle aged women and may precede thyroid disease. The hormone status in affected individuals ranges from hypothyroidism to a hyperthyroid state (in the context of Graves' disease). The acute presentation simulates cellulitis and clinically demonstrates injection and chemosis[25]. Exacerbations and remissions often follow the index presentation over a course of years. Thyroid orbitopathy is an immune mediated process and often exhibits a characteristic sequence of extra-conal muscle involvement as expected by the mnemonic I'M SLO (inferior rectus, medial rectus, superior rectus, lateral rectus and oblique muscles respectively)[26]. In fact isolated involvement of the lateral rectus or oblique muscles should prompt the search for an alternative diagnosis[13]. Muscular involvement is often bilateral and symmetrical and typically spares the muscle tendons resulting in fusiform enlargement of the muscles - the so called 'Coca-Cola bottle' sign. Coronal planes are preferred in both CT and MRI as they clearly demonstrate differential muscular involvement[27]. Unlike orbital pseudotumour the orbital fat is initially spared and the muscle-fat boundary remains well defined. The fat may be involved in later stages by the inflammatory process and

results in a 'dirty fat' appearance. Exophthalmos occurs as a result of both muscle enlargement and hypertrophy of the retro-orbital fat. 'Crowding' of the conal muscles at the apex may lead to venous congestion and compression of the optic nerve which may eventually lead to blindness. Imaging in thyroid eye disease is not only required as a diagnostic adjunct but also to monitor disease progression.

Hyperparathyroidism (figure 10) is associated with characteristic coarse calcifications typically seen at the corneo-scleral junction[28].

NEOPLASTIC

Choroidal melanoma (figure 11) represents the most common primary ocular neoplasm in adults and account for 3.1% of all melanomas[29]. Melanin within the lesion shortens the T1 relaxation time and the lesion therefore exhibits high signal intensity on T1 and low signal intensity on T2 weighted images. Melanoma appears hyperdense on CT and moderate contrast enhancement is often appreciated.

Ocular metastasis is the commonest intraocular malignancy[30] and preferentially affects the vascular-rich choroid membrane. Differential diagnoses include choroidal hemangioma, choroidal nevus, and primary intraocular lymphoma[31].

Imaging plays a crucial role in the evaluation of optic nerve neoplasms. Optic glioma (figure 12) may occur at any point along the optic tract. Histology and prognosis vary significantly according to the age at presentation. Pilocytic astrocytomas are childhood tumours which often follow an indolent course. In adults the neoplasms are higher grade astrocytomas (WHO grade III and IV neoplasms) and are associated with a dismal prognosis[13]. Up to 20% of patients with an optic nerve glioma will eventually be diagnosed with neurofibromatosis. Bilateral involvement is virtually diagnostic of neurofibromatosis type 1[32]. The neoplasm may be an incidental imaging finding, otherwise the patient may present with proptosis and disturbances of vision. Tubular or fusiform enlargement of the optic nerve is seen and 'kinking' of the nerve is characteristic. Widening of the optic canal may occur with intracanalicular extension of the neoplasm[33]. Enhancement is variable and reflects the pattern demonstrated by intracranial astrocytomas.

Optic nerve sheath meningioma (figure 13) has a slight female predilection and often presents in the fourth decade with retro-bulbar pain, and visual disturbances[34]. It is a benign tumour which accounts for up to 2% of intra-orbital neoplasms. Fusiform enlargement of the optic nerve sheath is seen on CT and MRI, and 'tram-track' enhancement along the sheath is characteristic[35]. CT findings reflect those of intracranial meningiomas with the tumour appearing hyperdense and psammomatous calcifications are present in up to half of the cases. Differential diagnoses include sarcoidosis, Wegener's granulomatosis, and metastatic infiltration[31].

Lymphoma (figure 14) may involve any orbital compartment but the lacrimal glands are the commonest site involved. It presents with painless proptosis and visual

disturbances and the mean age at presentation is 63 years. The orbit is usually involved secondarily as part of systemic non-Hodgkin's lymphoma[36]. Lymphoma appears hyperdense on CT and is of low signal intensity on both T1 and T2 weighted MRI[31]. Avid enhancement occurs in the post contrast sequences. Lymphoma is a pliable tumour and characteristically crosses the compartmental boundaries. Bone erosion is not a feature.

Lacrimal gland neoplasms often present with exophthalmos, ptosis and diplopia. Adenoid cystic carcinoma (figure 15) is the commonest lacrimal gland malignancy[37] and often presents in the fourth decade. The tumour is irregularly marginated and may cause erosion of the adjacent bone. On MRI it displays a heterogeneous signal, and moderate to strong contrast enhancement is appreciated. Benign lesions include benign mixed tumours (BMT), pleomorphic adenomas, lacrimal cysts (figure 16) and dermoids. Differentiation from malignant lesions is not straightforward and biopsy is often needed to confirm the diagnosis.

Basal cell (figure 17) and squamous cell carcinomas are the commonest cutaneous lesions[38] that involve the orbit and often occur in the region of the medial canthus.

Metastases commonly involve the orbit. Breast and renal cell carcinomas (figure 18) are the commonest primary malignancies in adulthood whereas neuroblastoma metastasis (figure 19) is responsible for the majority of pediatric cases.

PARANASAL SINUSES

Secondary orbital involvement from paranasal sinus disease is not uncommon. Post-septal cellulitis can complicate aggressive paranasal sinus infections[39] and often reflects breach of the bony orbital contour. Mucocoeles (figure 20) and inverted papillomas[40] may also project into the orbital cavity, and should be included in the differential diagnosis of extra-conal etiologies especially in patients with a history of atopia.

BONE

As previously discussed in the anatomy section, the orbital cavity is a complex bony structure and hence any osseous pathology may affect the orbital contours and even project into the cavity. Fibrous dysplasia (figure 21) typically causes bone expansion with a characteristic ground glass matrix resulting in deformity of the orbital cone. The condition therefore affects the extra-conal compartment and often presents with unilateral (or less commonly bilateral) exophthalmos.

Hyperostosis associated with sphenoid wing meningiomas (figure 22) can present in a similar fashion. Dysplasia of the greater wing of the sphenoid seen with neurofibromatosis type-1 (figure 23) also results in orbital deformity[41].

TRAUMA

Injuries to the globe may be penetrating[42] (figure 24 and figure 25) or non-penetrating (figures 26 and 27) in nature. Orbital injury includes a whole spectrum of fracture patterns. The 'blow-out' type of fracture (figure 28) is caused by a sudden increase in intra-orbital pressure which forces the intra-orbital fat inferiorly through the roof of the maxillary sinus.

Foreign bodies are a common occurrence in everyday radiological practice. Management depends on the affected compartment (figure 29), and the mechanism of injury[43]. Previous ocular injury may result in a scarred non-functional globe also known as phthisis bulbi (figure 30). Imaging findings include curvilinear choroido-scleral calcifications and clumps of dystrophic calcifications within the vitreous humor.

IATROGENIC / CONGENITAL

Prosthetic implants (figure 31), deformity resulting from exenteration (figure 32) and changes related to previous cataract surgery (figure 33) could present interpretation confounds unless a previous surgical history is available. Congenital ocular malformations including optic disc drusen (figure 34), coloboma (figure 35) and staphyloma (figure 36) are occasional incidental imaging findings in adults.

CONCLUSION

Sound anatomical knowledge is imperative when dealing with orbital and ocular pathology. The orbital compartment primarily involved needs to be identified and clinical input is often necessary to further narrow the differential diagnosis. Biopsy is nonetheless required in some instances when clinical and radiological findings are equivocal.

TEACHING POINT

The etiology of orbital pathology is protean and therefore clinical input is often necessary to narrow the differential diagnosis. In this pictorial review we classify ocular and orbital pathology in major etiological categories whilst attempting to highlight characteristic imaging findings.

REFERENCES

1. Soanes C, Stevenson A, Pearsall J, Hanks P. Oxford Dictionary Of English. Oxford: Oxford University Press, 2005; 2005.
2. Miloro M, Ghali G, Larsen P, Waite P. Peterson's Principles Of Oral And Maxillofacial Surgery. Hamilton, Ont.; London: BC Decker Inc., 2004.; 2004.

3. Aviv RI, Casselman J. Pictorial Review: Orbital imaging: Part 1. Normal anatomy. *Clinical Radiology* 2005;60:279-287. PMID: 15710133.
4. Forbes G. Vascular lesions in the orbit. *Neuroimaging Clin N Am* 1996;6(1):113-122. PMID: 8919137.
5. Harris GJ. Orbital vascular malformations: a consensus statement on terminology and its clinical implications. *Orbital Society. Am J Ophthalmol.* 1999 Apr;127(4):453-5. PMID: 10218699.
6. Mulliken Jb, Glowacki J. Hemangiomas and vascular malformations in infants and children: a classification based on endothelial characteristics. *Plast Reconstr Surg* 1982;69:412-422. PMID: 7063565.
7. Smoker WR, Gentry LR, Yee NK, Reede DL, Nerad JA. Vascular lesions of the orbit: more than meets the eye. *Radiographics.* 2008 Jan-Feb;28(1):185-204. PMID: 18203938.
8. Haik BG, Karcioğlu ZA, Gordon RA, Pechous BP. Capillary hemangioma (infantile periorbital hemangioma). *Surv Ophthalmol* 1994;38(5):399-426. PMID: 8009426.
9. Bilaniuk LT. Orbital vascular lesions: role of imaging. *Radiol Clin North Am* 1999;37:169-183. PMID: 10026736.
10. Vu BL, Harris GJ. Orbital vascular lesions. *Ophthalmol Clin North Am* 2000;13:609-631.
11. Dubois J, Garel L. Imaging and therapeutic approach of hemangiomas and vascular malformations in the pediatric age group. *Pediatr Radiol* 1999;29(12):879-893. PMID: 10602864.
12. Bilaniuk LT. Vascular lesions of the orbit in children. *Neuroimaging Clin N Am* 2005;15(1):107-120. PMID: 15927863.
13. Aviv RI, Miszkil K. Pictorial Review: Orbital imaging: Part 2. Intraorbital pathology. *Clinical Radiology* 2005;60:288-307. PMID: 15710134.
14. Katz S, Rootman J, Vangveeravong S, Graeb D. Combined venous lymphatic malformations of the orbit (so-called lymphangiomas). Association with noncontiguous intracranial vascular anomalies. *January 1998;105(1):176-184.* PMID: 9442796.
15. Ponce F, Han P, Spetzler R, Canady A, Feiz-Erfan I. Associated arteriovenous malformation of the orbit and brain: a case of Wyburn-Mason syndrome without retinal involvement - Case report. *Journal Of Neurosurgery* Aug 2001;95(2):346-349. PMID: 11780909.
16. P.S. Goh, A. Charlton, C. Tan, J.K. Gangadhara Sundar, S. Amrith. Review: Review of orbital imaging. *European Journal Of Radiology.* 2008;66(Head - Neck Cancer):387-395. PMID: 18501542.
17. Hamid R, Tanveer-ul-Haq, Shamim M, Kazim S, Salam B. Endovascular approach as primary treatment for traumatic carotid cavernous fistula: local experience from Pakistan. *Journal Of The Pakistan Medical Association;*61(10):989-993. PMID: 22356033.
18. Botting AM, McIntosh D, Mahadevan M. Paediatric pre- and post-septal peri-orbital infections are different diseases. A retrospective review of 262 cases. *International Journal Of Pediatric Otorhinolaryngology.* 2008;72:377-383. PMID: 18191234.
19. Kandpal H, Vashisht S, Sharma R, Seith A. Imaging spectrum of pediatric orbital pathology: A pictorial review. *Indian Journal Of Ophthalmology* December 2006;54(4):227-236. PMID: 17090873.
20. Padhi T, Basu S, Das T, Samal B. Optic disc tuberculoma in a patient with miliary tuberculosis. *Ocular Immunology And Inflammation.* February 2011;19(1):67-68. PMID: 21054196.
21. Sobol G, Mizia A, Musiol K, Pajak J, Madera-Buchta T, Wos H. Orbital pseudotumour imitating a proliferative process. *Medycyna Wieku Rozwojowego.* July 2005;9(3 Pt 2):561-566. PMID: 16719169.
22. Ding ZX, Lip G, Chong V. Pictorial Review: Idiopathic orbital pseudotumour. *Clinical Radiology* 2011;66:886-892. PMID: 21546008.
23. Pau D, Al Zubidi N, Yalamanchili S, Plant G, Lee A. Optic neuritis. *Eye (London, England).* July 2011;25(7):833-842. PMID: 21527960.
24. Burman J, Raininko R, Fagius J. Bilateral and recurrent optic neuritis in multiple sclerosis. *Acta Neurologica Scandinavica.* March 2011;123(3):207-210. PMID: 20569226.
25. Cockerham K, Chan S. Thyroid eye disease. *Neurologic Clinics.* August 2010;28(3):729-755. PMID: 20637998.
26. Dähnert W. *Radiology Review Manual.* Philadelphia : Lippincott Williams & Wilkins, c2003.; 2003.
27. Lee A, Johnson M, Policeni B, Smoker W. Imaging for neuro-ophthalmic and orbital disease - a review. *Clinical & Experimental Ophthalmology* January 2009;37(1):30-53. PMID: 19016810.
28. Grech R, Grech S, Mizzi A. Intracranial Calcifications: A Pictorial Review. *Neuroradiology Journal,* August 2012;25(4):427. PMID: 24029036
29. Singh A, Turell M, Topham A. Uveal melanoma: trends in incidence, treatment, and survival. *Ophthalmology.* September 2011;118(9):1881-1885. PMID: 21704381.
30. Ahmad SM, Bsmaeli B. Metastatic tumors of the orbit and ocular adnexa. *Curr Opin Ophthalmol* 2007;18:405-13. PMID: 17700235.

31. Mysore N, Gonçalves F, Chankowsky J, del Carpio-O'Donovan R. Adult orbital masses: a pictorial review. *Canadian Association Of Radiologists Journal* February 2012;63(1):39-46. PMID: 21273028.
32. Shapey J, Danesh-Meyer HV (b c, Kaye AH. Review: Diagnosis and management of optic nerve glioma. *Journal Of Clinical Neuroscience*. 2011;18:1585-1591. PMID: 22071462.
33. Duane T, Tasman W, Jaeger E. *Duane's Ophthalmology*. Editors, William Tasman, Edward A. Jaeger. Hagerstown, MD : Lippincott Williams & Wilkins, 2010.; 2010.
34. Savino P, Danesh-Meyer H. *Neuro-ophthalmology: colour atlas & synopsis of clinical ophthalmology*. New York: McGraw-Hill: 2(X)3.
35. De Potter P, Flanders AE, Shields CL. et al. Magnetic resonance imaging of orbital tumors. *Int Ophthalmol Clin* 1993;33:163-72. PMID: 8407182.
36. Haque S, Law M, Abrey LE. et al. Imaging of lymphoma of the central nervous system, spine, and orbit. *Radiol Clin N Am* 2(X)8;46;339-61. PMID: 18619384.
37. Snaathorst J, Sewnaik A, Paridaens D, de Krijger RR, van der Meij EH. Clinical Paper: Primary epithelial tumors of the lacrimal gland; a retrospective analysis of 22 patients. *International Journal Of Oral & Maxillofacial Surgery*. 2009;38:751-757. PMID: 19369032.
38. Proia A, Selim M, Reutter J, Michon J. Basal cell-signet-ring squamous cell carcinoma of the eyelid. *Archives Of Pathology & Laboratory Medicine*. March 2006;130(3):393-396. PMID: 16519572.
39. Kastner J, Taudy M, Lisy J, Grabec P, Betka J. Orbital and intracranial complications after acute rhinosinusitis. *Rhinology*. December 2010;48(4):457-461. PMID: 21442085.
40. Kim Y, Kim K, Lee J, Yoon J, Kim C. Paranasal sinus mucoceles with ophthalmologic manifestations: a 17-year review of 96 cases. *American Journal Of Rhinology & Allergy*. July 2011;25(4):272-275. PMID: 21819766.
41. Friedrich R, Stelljes C, Hagel C, Giese M, Scheuer H. Dysplasia of the Orbit and Adjacent Bone Associated with Plexiform Neurofibroma and Ocular Disease in 42 NF-1 Patients. *Anticancer Research*. May 2010; 30(5):1751-1764. PMID: 20592374.
42. Agrawal R, Rao G, Naigaonkar R, Ou X, Desai S. Prognostic factors for vision outcome after surgical repair of open globe injuries. *Indian Journal Of Ophthalmology*. November 2011;59(6):465-470. PMID: 22011491.
43. Mukherjee B, Goel S, Subramanian N. An unusual case of intraorbital foreign body and its management. *Indian Journal Of Ophthalmology*. January 2011;59(1):58-60. PMID: 21157077.

FIGURES

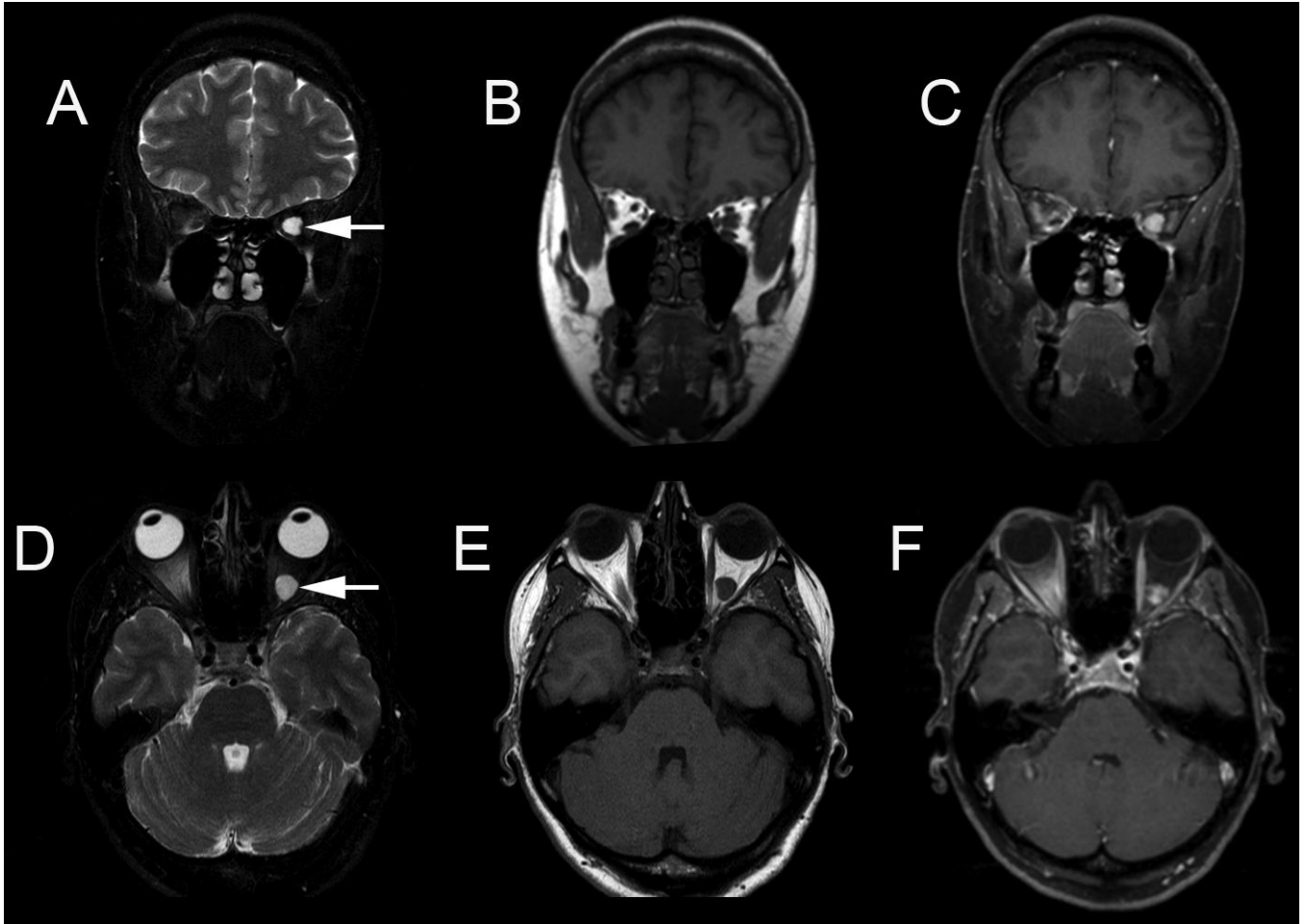


Figure 1: Capillary hemangioma in an asymptomatic 50 year old female. A well circumscribed intra-conal lesion is seen which displays marked homogenous T2 hyperintensity (arrows - images A and D). The lesion is isointense to grey matter on T1 (images B and E), and demonstrates typical avid enhancement on the fat suppressed post contrast sequences (images C and F). (Protocol: Siemens Symphony 1.5T MRI. Image A: Coronal T2, TR/TE - 4690/109ms , 4mm slice thickness, 512 x 250 matrix, non-contrast. Image B: Coronal T1, TR/TE - 473/12ms , 4mm slice thickness, 256 x 192 matrix, non-contrast. Image C: Coronal T1, TR/TE - 426/12ms , 4mm slice thickness, 256 x 192 matrix, Gadavist: 0.1 mmol/kg . Image D: Axial T2, TR/TE - 4950/95ms , 4mm slice thickness, 512 x 218 matrix, non-contrast. Image E: Axial T1, TR/TE - 523/14ms , 3mm slice thickness, 512 x 250 matrix, non-contrast. Image F: Coronal T1, TR/TE - 644/12ms , 3mm slice thickness, 256 x 192 matrix, Gadavist: 0.1 mmol/kg.)

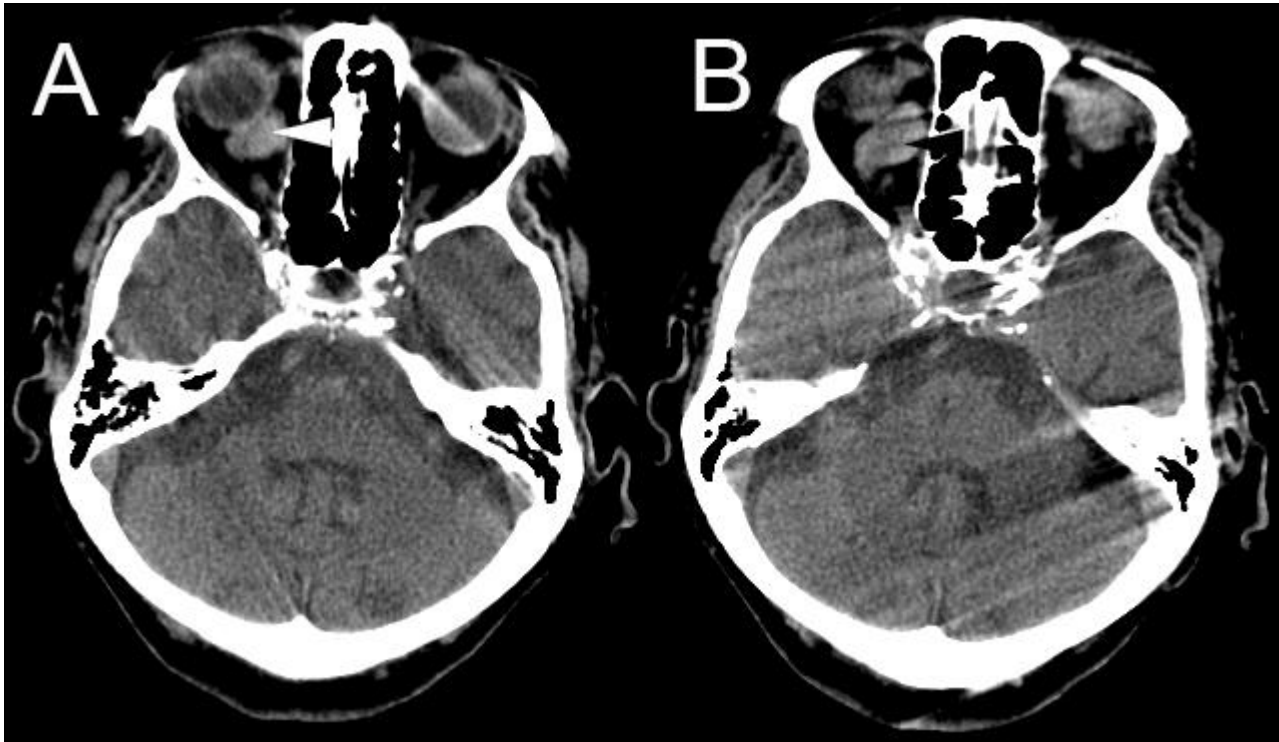


Figure 2: Orbital varix in a 84 year old female. Contiguous contrast enhanced CT images demonstrate an engorged tubular channel (arrowheads) which characteristically tapers towards the orbital apex. No internal septations are seen. The diagnosis of orbital varix was confirmed on Doppler ultrasound which showed low-velocity flow with increase in size following Valsalva maneuver.

(Protocol: GE BrightSpeed Elite 16 Slice CT at 140mA and 120kV, 5mm slice thickness, non contrast).

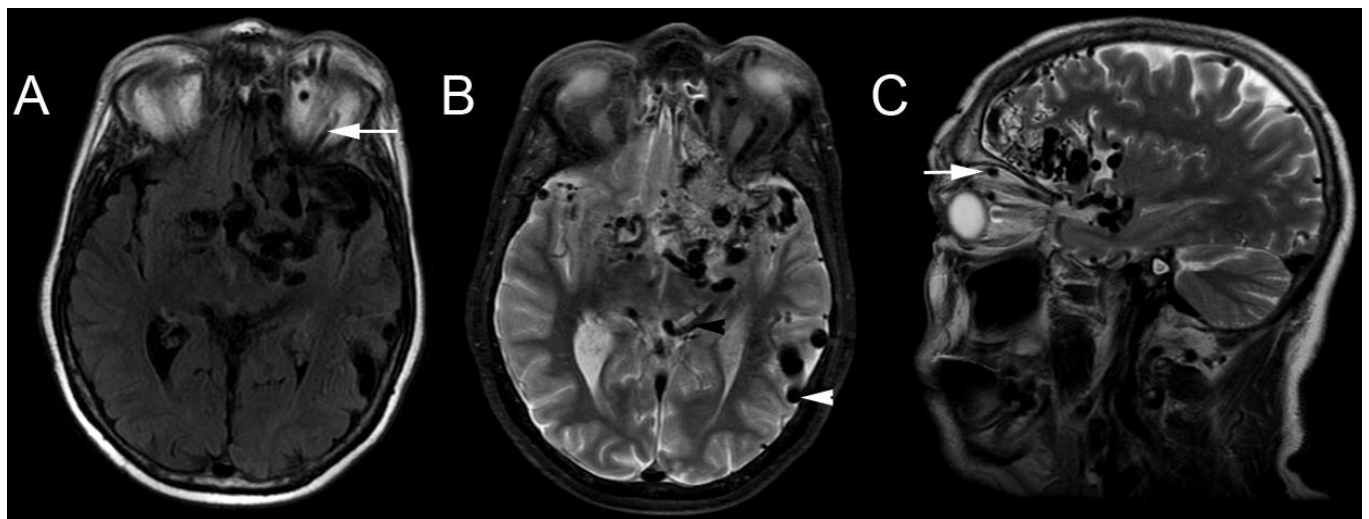


Figure 3: Martin-Spezler grade 5 left frontal arteriovenous malformation (AVM) in a 64 year old male. The AVM is seen as a cluster of signal voids on axial FLAIR (image A), axial and sagittal T2 (images B and C respectively) weighted sequences. The increased venous pressure causes engorgement of the superior orbital veins (arrows) likely responsible for the patient's main complaint of retro-orbital pressure sensation. Venous drainage to both deep (black arrowhead) and superficial cortical veins (white arrowhead) is noted.

(Protocol: GE Signa EXCITE 1.5T MRI. Image A: Axial FLAIR, TR/TE - 8502/163ms , 4mm slice thickness, 320 x 224 matrix, non-contrast. Image B: Axial T2, TR/TE - 6000/33ms , 6mm slice thickness, 512 x 256 matrix, non-contrast. Image C: Sagittal T2, TR/TE - 5000/94ms , 5mm slice thickness, 384 x 256 matrix, non-contrast.)

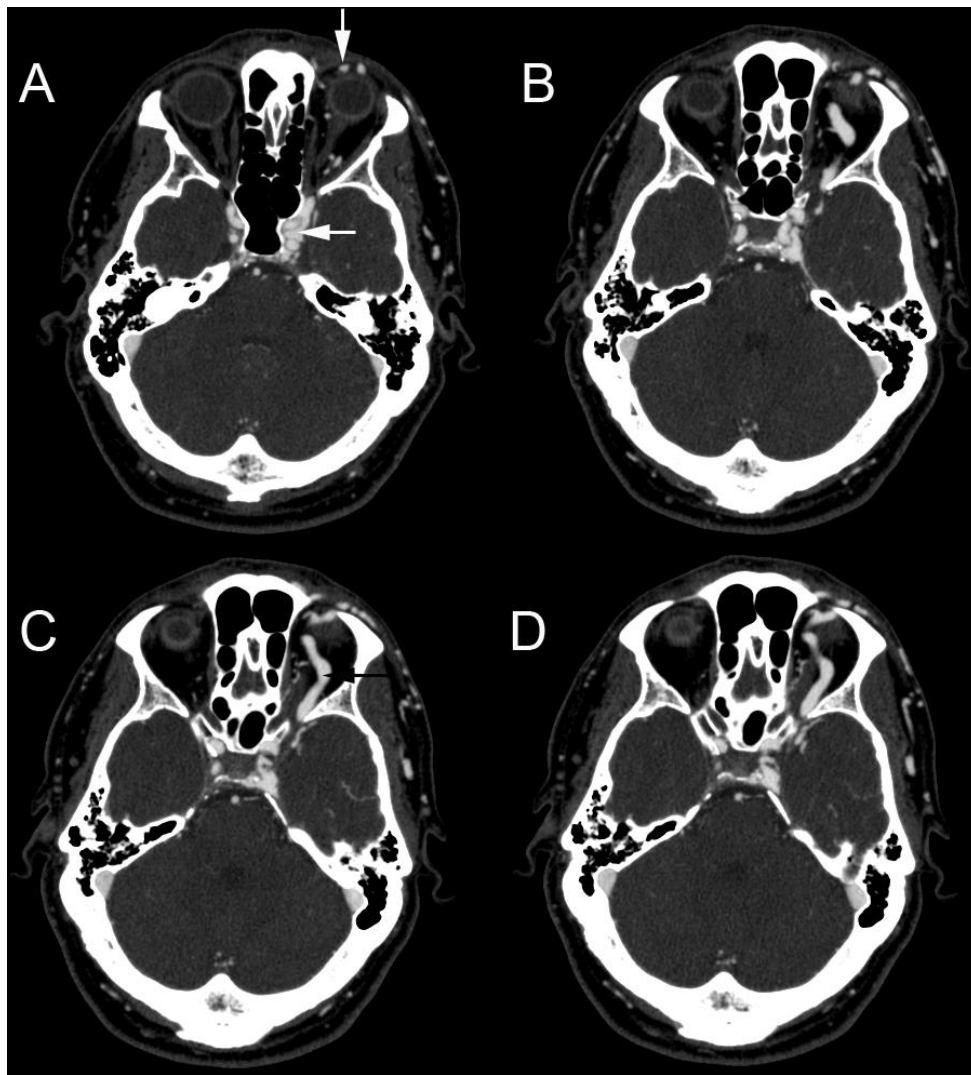


Figure 4: Carotico-cavernous fistula in a 55 year old male who presented with chemosis, pulsatile exophthalmos and an orbital bruit. Stack of contrast enhanced axial CT images showing prominent left orbital veins (in the superior extra-conal compartment) draining into an engorged left cavernous sinus (white arrows). The left superior ophthalmic vein (black arrow) best seen in image C is tortuous and dilated. The constellation of findings is pathognomonic for carotico-cavernous fistula. (Protocol: GE BrightSpeed Elite 16 Slice CT, at 400mA and 120kV, 0.6mm slice thickness, Omnipaque 300 - 50mls i.v.).

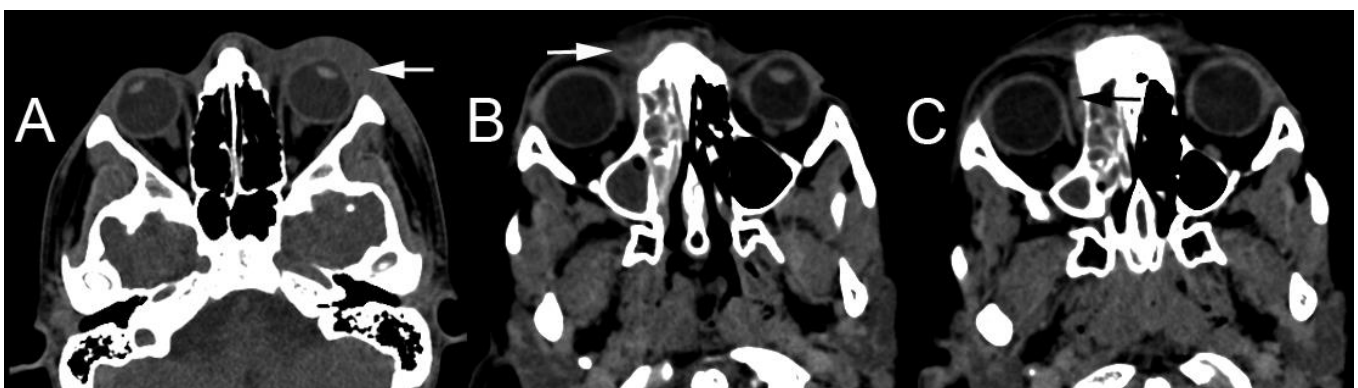


Figure 5: Pre-septal orbital cellulitis (image A) in a 19 year old male seen as soft tissue swelling (white arrow) and adjacent fat stranding on this non-enhanced axial CT. Images B and C are from a 25 year old female who presented with chronic sinusitis and orbital cellulitis complicated by post-septal extension and formation of a sub-periosteal abscess (black arrow). Note the opacification of the right maxillary and ethmoidal air cells in images B and C. (Protocol: Image A: Siemens Sensation 16 Slice CT, at 215mA and 120kV, 1mm slice thickness, non contrast. Image B: GE BrightSpeed Elite 16 Slice CT, at 134mA and 120kV, 2mm slice thickness, non contrast).



Figure 6: Choroidal tuberculoma in a 22 year old immunocompromised male with a past history of primary pulmonary tuberculosis. Sequential contrast enhanced axial CT images in a cranio-caudal direction (images A to C) demonstrate an ill defined lesion in the posterolateral aspect of the left globe. Ophthalmic examination revealed an elevated choroidal lesion and a diagnosis of choroidal tuberculoma was proposed. The lesion size decreased dramatically following the administration of anti-tuberculous treatment.

(Protocol: Siemens Sensation 16 Slice CT, at 185mA and 120kV, 1mm slice thickness, Omnipaque 300 - 70mls i.v.).

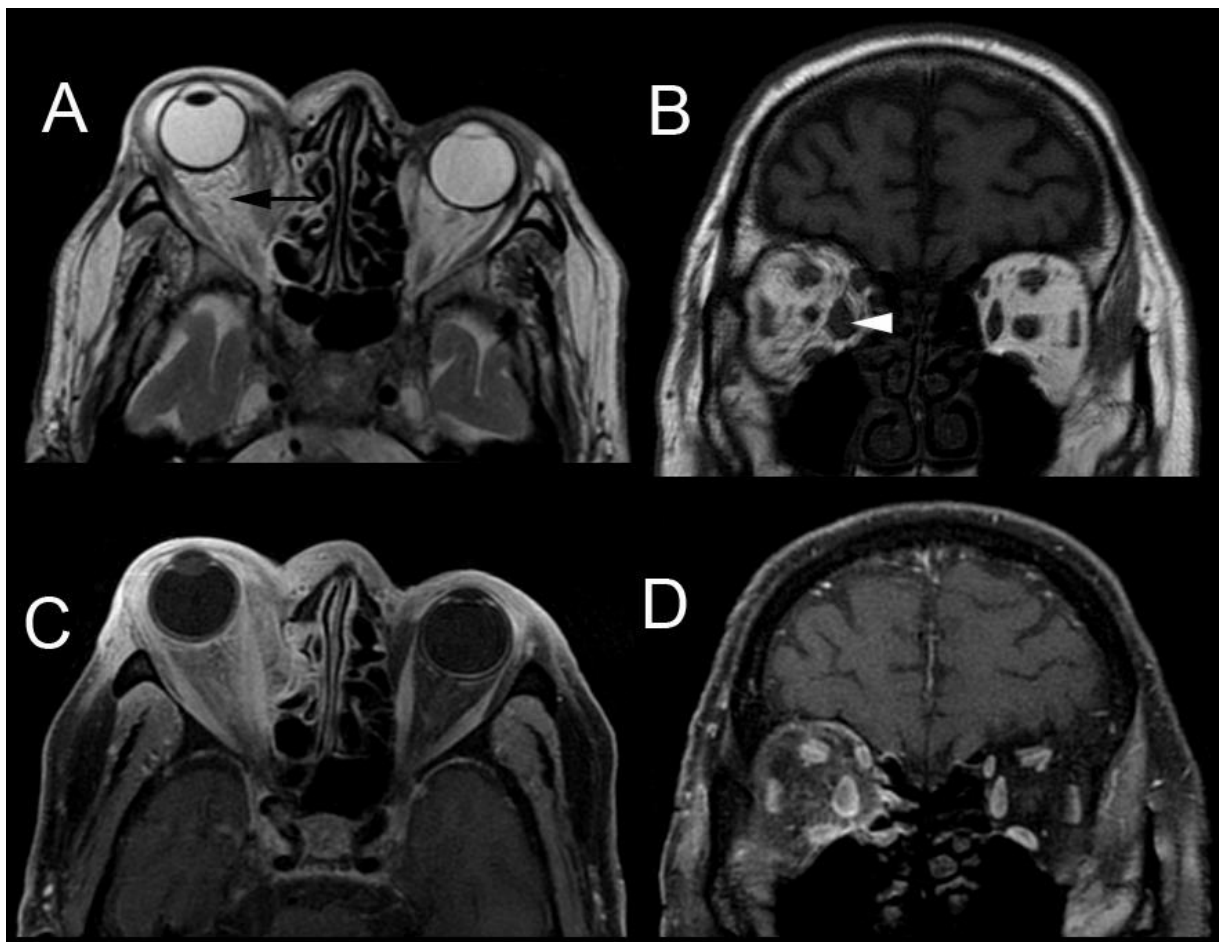


Figure 7: Orbital pseudotumour in a 77 year old male who presented with painful unilateral exophthalmos. Axial (images A and C) and coronal (images B and D) orbital MR images reveal a diffuse inflammatory process involving the retro-bulbar fat (arrow) and the conal muscles (arrowhead) which causes right-sided proptosis (appreciated better on the axial images). The fat stranding gives a 'dirty fat' appearance (arrow) and mild enhancement is seen following the administration of contrast (image D). The imaging appearances are non-specific and orbital pseudotumour remains a diagnosis of exclusion.

(Protocol: GE Signa EXCITE 1.5T MRI . Image A: Axial T2, TR/TE - 4400/76ms , 3mm slice thickness, 256 x 224 matrix, non-contrast. Image B: Coronal T1, TR/TE - 420/12ms , 3mm slice thickness, 288 x 256 matrix, non-contrast. Image C: Axial T1, TR/TE - 580/10ms , 3mm slice thickness, 256 x 224 matrix, Gadavist: 0.1 mmol/kg. Image D: Coronal T1, TR/TE - 580/10ms , 3mm slice thickness, 256 x 224 matrix, Gadavist: 0.1 mmol/kg.)

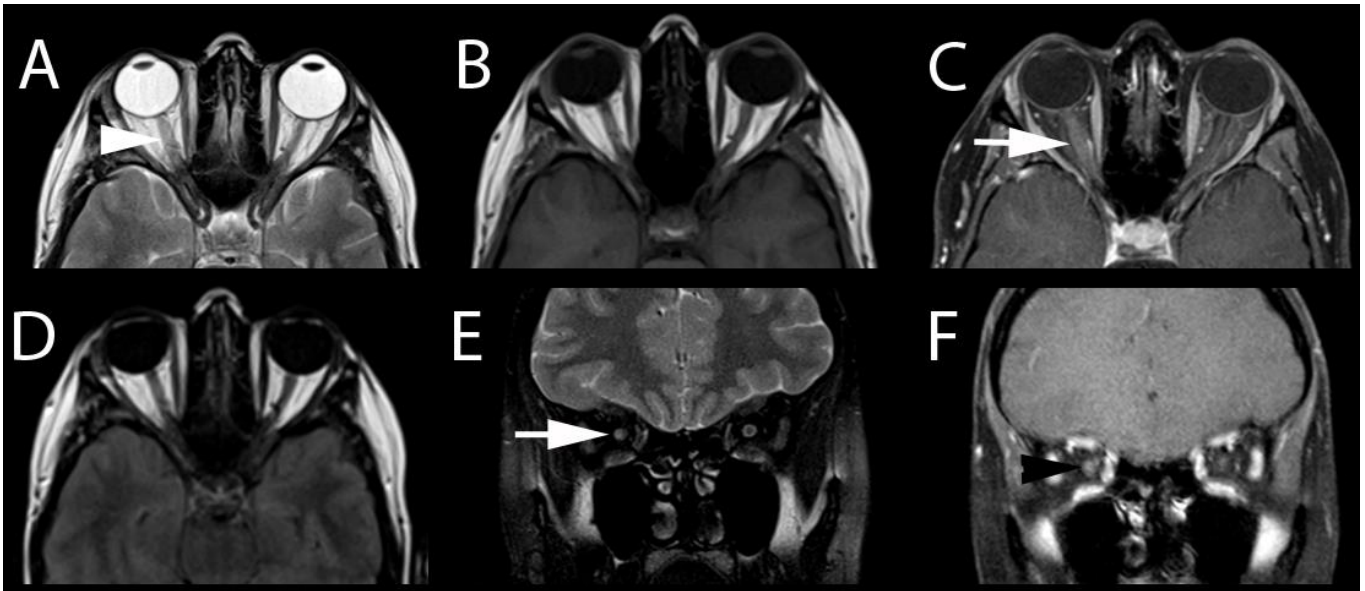


Figure 8: 28 year old woman with a first episode of optic neuritis, who presented with acute onset of right eye pain and vision decline. The diagnosis was made clinically and MRI was performed as part of a full multiple sclerosis workup. The right optic nerve is relatively swollen compared to the left and has a focus of increased signal on T2 weighted imaging (arrowhead - image A). Pre- and post- contrast T1 axial (images B and C) and coronal (images E and F respectively) sequences demonstrate fusiform swelling of the right optic nerve with definite enhancement of the intra-orbital portion. Increased signal within the optic nerve is also seen on the FLAIR sequence (image D).

(Protocol: MAGNETOM Symphony TIM 1.5T MRI. Image A: Axial T2, TR/TE - 4500/97ms , 5mm slice thickness, 448 x 306 matrix, non-contrast. Image B: Axial T1, TR/TE - 550/9ms , 5mm slice thickness, 256 x 256 matrix, non-contrast. Image C: Axial T1, TR/TE - 699/17ms , 3mm slice thickness, 320 x 240 matrix, Gadavist: 0.1 mmol/kg. Image D: Axial FLAIR, TR/TE - 9340/156ms , 5mm slice thickness, 256 x 204 matrix, non-contrast. Image E: Coronal T1, TR/TE - 699/17ms , 3mm slice thickness, 320 x 240 matrix, non-contrast. Image F: Coronal T1, TR/TE - 699/17ms , 3mm slice thickness, 320 x 240 matrix, Gadavist: 0.1 mmol/kg.)

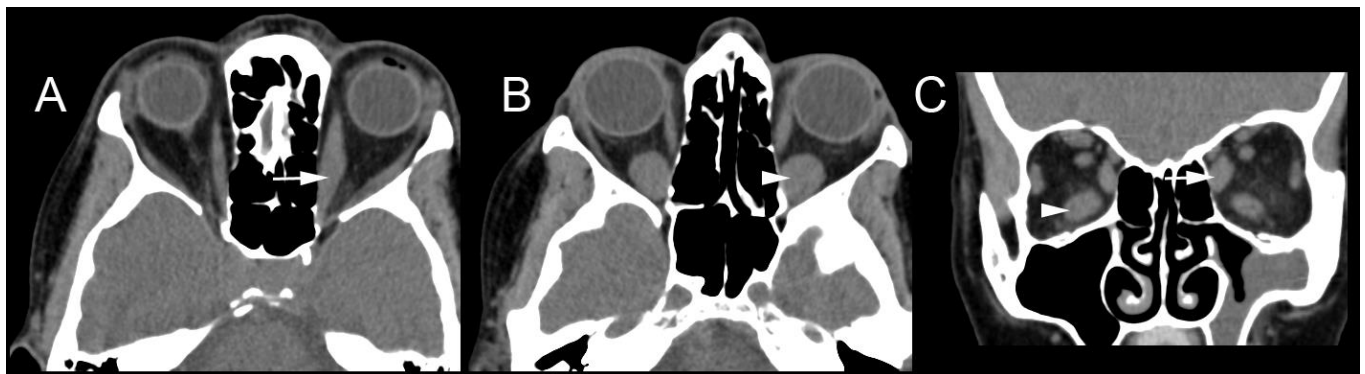


Figure 9: Thyroid orbitopathy in a 58 year old female. Axial (images A and B) and reconstructed coronal (image C) CT images show bilateral exophthalmos. The medial (arrow) and inferior recti muscles are enlarged and symmetrically affected (as seen on the coronal image). Mild retro-bulbar fat stranding is noted bilaterally. The muscle tendons are spared resulting in a characteristic 'Coca-Cola bottle' sign (arrow). The radiological appearances are characteristic of thyroid orbitopathy.

(Protocol: Siemens Sensation 16 Slice CT, at 179mA and 120kV, 1mm slice thickness, non contrast).

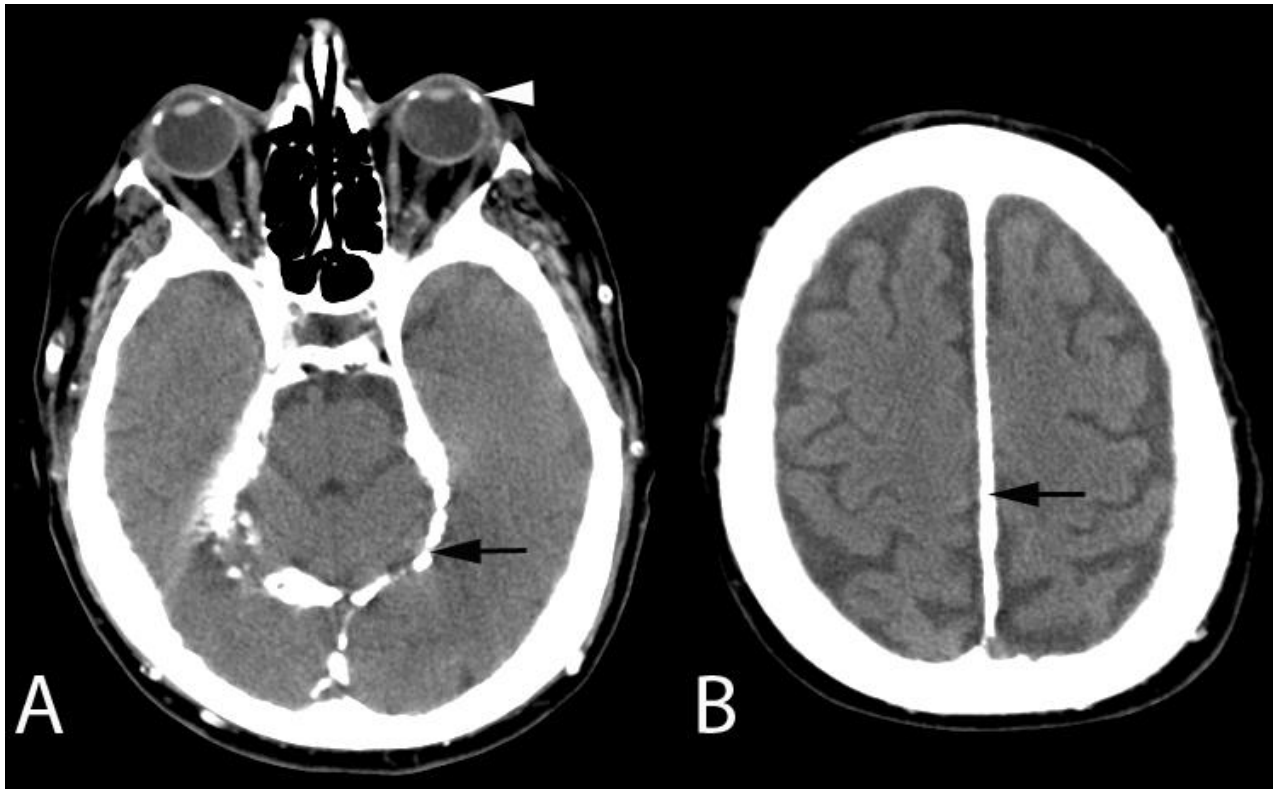


Figure 10: Axial non-enhanced CT images in a 45 year old male patient with hyperparathyroidism. Characteristic coarse calcifications are seen at the corneo-scleral junctions (arrowhead - image A). Heavy linear calcifications of the falx cerebri and tentorium cerebelli (arrows) are also seen.

(Protocol: GE BrightSpeed Elite 16, at 118mA and 120kV, 2mm slice thickness, non contrast).



Figure 11 (left): Choroidal melanoma in a 64 year old female. Non-enhanced axial CT image showing an oval shaped hyperdense choroidal lesion in the medial aspect of the right globe (arrowhead). Fine-needle biopsy confirmed a primary choroidal melanoma. There was no evidence of metastatic spread following imaging for staging workup.

(Protocol: Siemens Definition AS 128 Slice CT, at 99mA and 120kV, 1mm slice thickness, non contrast).

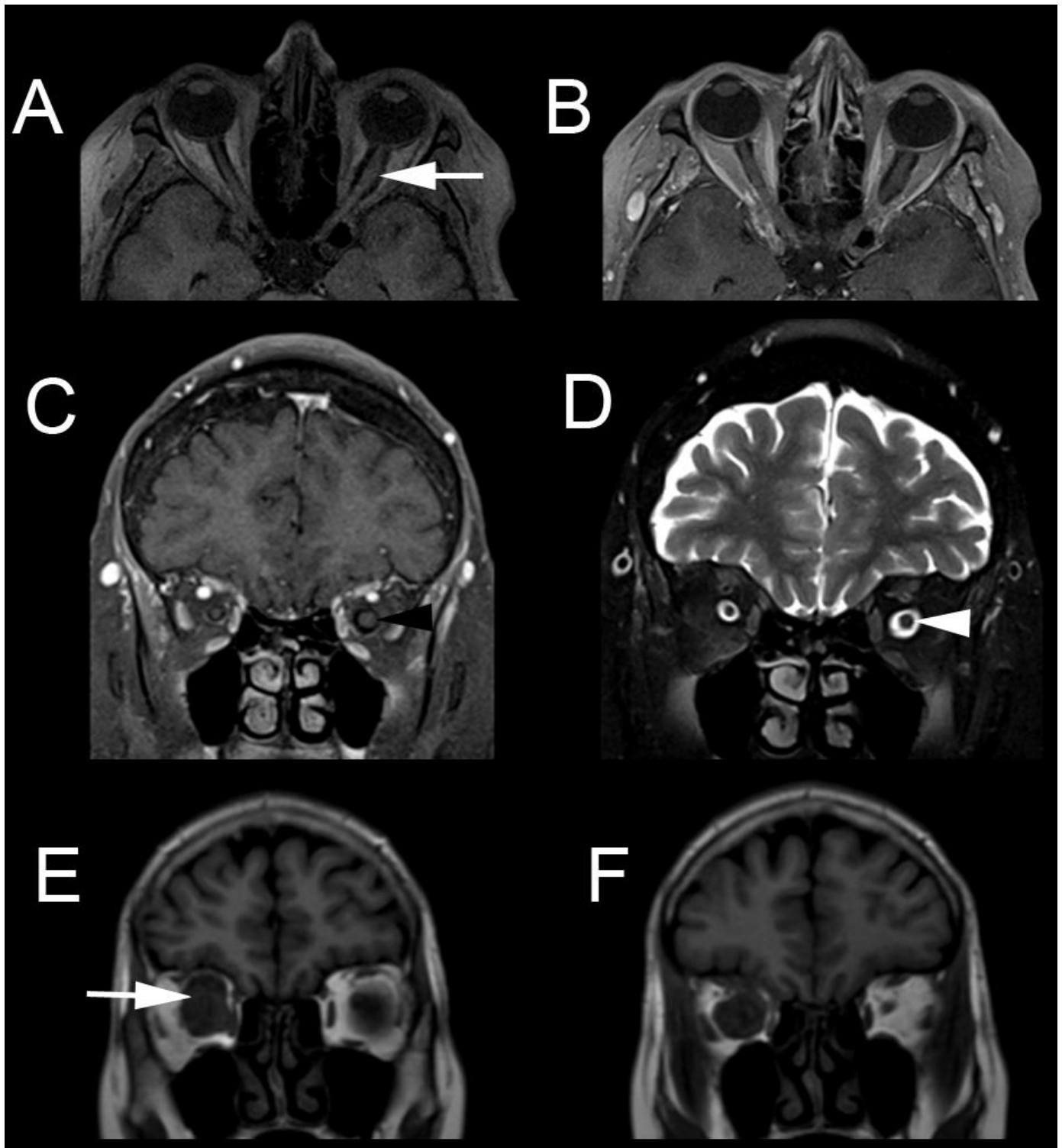


Figure 12: 68 year old female with a known diagnosis of neurofibromatosis type-1, who presented with a short history of decreased left eye vision. Pre- and post-contrast axial T1 sequences (images A and B respectively) demonstrate asymmetrical enlargement of the intra-orbital portion of left optic nerve (arrow) with no significant enhancement. Coronal T1 and T2 weighted images (C and D) show increased cross sectional area of the affected nerve (arrowhead), with increased central T2 signal. The optic chiasm is uninvolved. Images E and F are from a 43 year old man with mild right sided proptosis and deteriorating vision. Sequential T1 coronal images show a massively enlarged right optic nerve (arrow). The diagnosis of optic nerve glioma was confirmed histologically in both patients.

(Protocol: Images A-D: Siemens MAGNETOM Avanto 1.5T MRI. Image A: Coronal T2, TR/TE - 382/9ms , 3mm slice thickness, 384 x 216 matrix, non-contrast. Image B: Axial T1, TR/TE - 382/9ms , 3mm slice thickness, 384 x 216 matrix, Gadavist: 0.1 mmol/kg. Image C: Coronal T1, TR/TE - 474/8ms , 3mm slice thickness, 256 x 144 matrix, Gadavist: 0.1 mmol/kg. Image D: Coronal T2, TR/TE - 4180/100ms , 3mm slice thickness, 320 x 180 matrix, non-contrast. Images E & F: GE Signa EXCITE 1.5T MRI. Coronal T1, TR/TE - 2253/9ms , 5mm slice thickness, 256 x 224 matrix, non-contrast.)

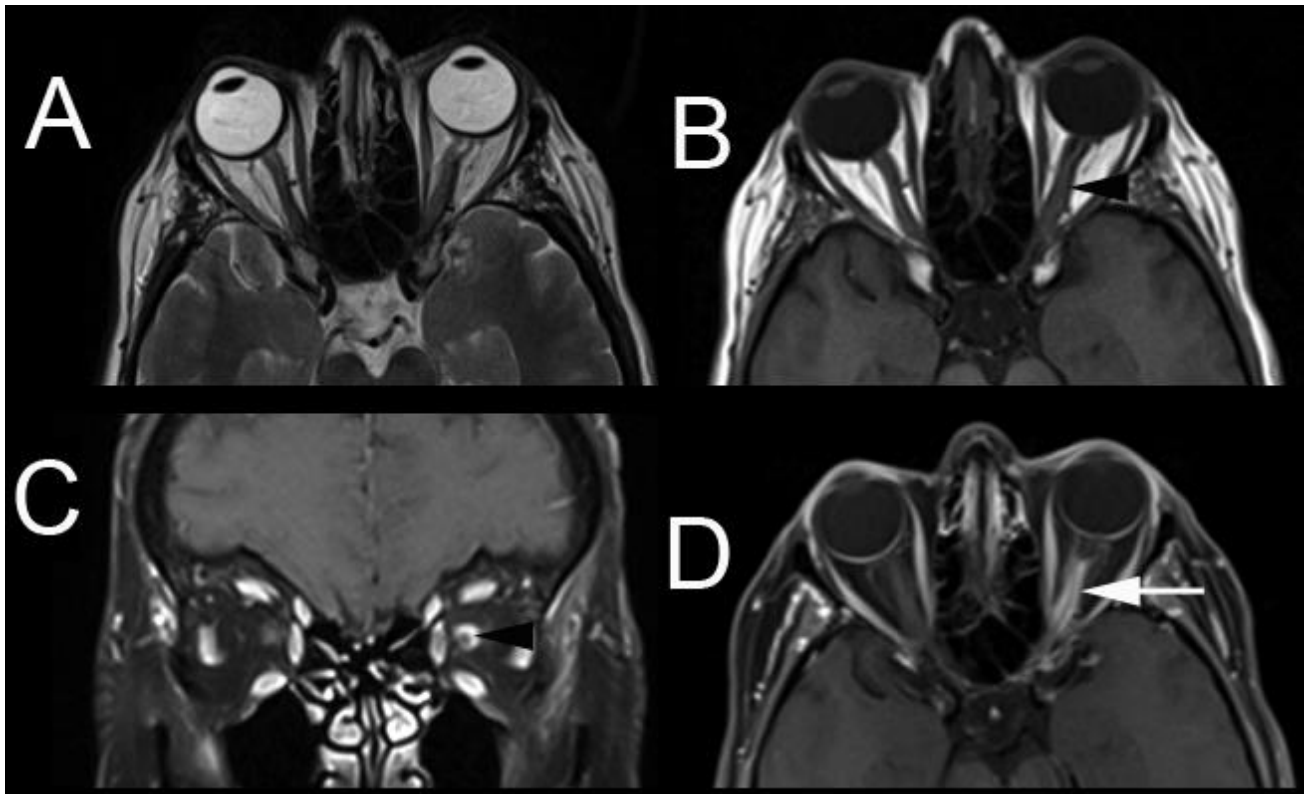


Figure 13: Incidental optic nerve sheath meningioma in a 55 year old female. Fusiform enlargement of the left optic nerve (arrowheads) is seen on axial T2 (image A) and T1 (image B) weighted images. Avid circumferential enhancement of the optic nerve sheath is demonstrated on the contrast enhanced coronal T1 sequence (image C) resulting in characteristic 'tram-track' enhancement (arrow - image D).

(Protocol: Siemens MAGNETOM Avanto 1.5T MRI. Image A: Axial T2, TR/TE - 5000/89ms, 5mm slice thickness, 384 x 261 matrix, non contrast. Image B: Axial T1, TR/TE - 500/8ms, 3.5mm slice thickness, 256 x 224 matrix, non contrast. Image C: Coronal T1, TR/TE - 538/9ms, 4mm slice thickness, 384 x 216 matrix, Gadavist: 0.1 mmol/kg. Image D: Axial T1, TR/TE - 500/11ms, 3.5mm slice thickness, 256 x 209 matrix, Gadavist: 0.1 mmol/kg.)



Figure 14: Biopsy proven non-Hodgkin's lymphoma in a 48 year old female patient who presented with symptoms secondary to obstruction of the right nasolacrimal duct. An ill defined soft tissue density lesion is seen at the infero-medial aspect of the right orbit (arrow - image A). There is no evidence of associated bone destruction (image B).

(Protocol: Siemens Sensation 16 Slice CT, at 50mA and 120kV, 1mm slice thickness, Omnipaque 300 - 50mls i.v.).

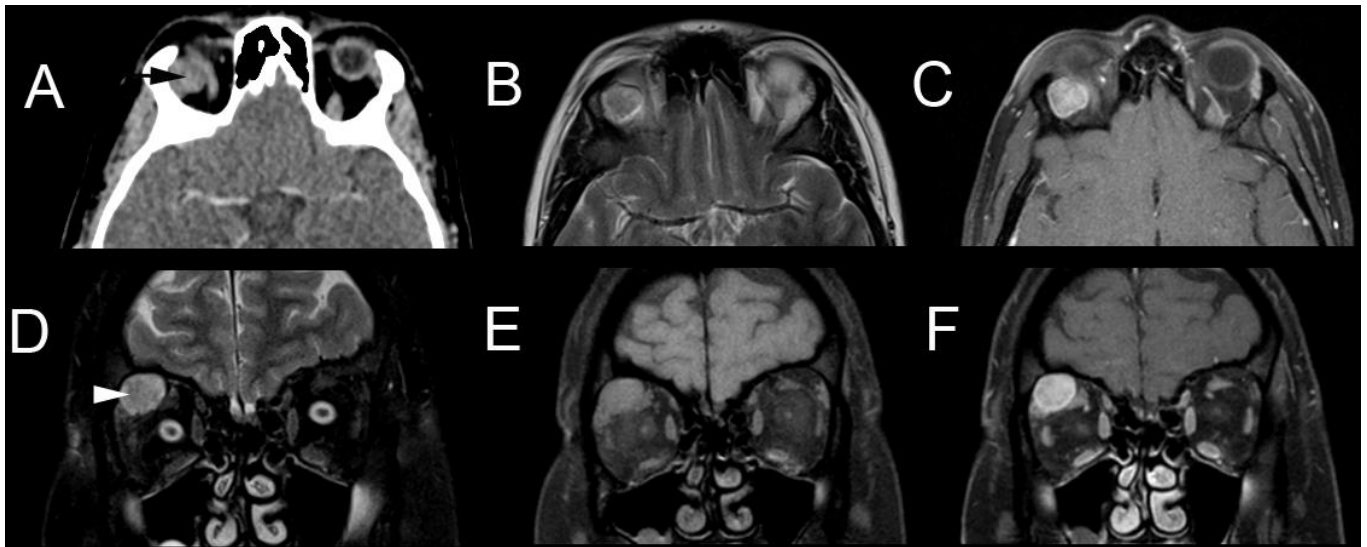


Figure 15: Adenoid cystic carcinoma of the lacrimal gland in a 33 year old female, who presented with exophthalmos and diplopia. The lesion is isointense to muscle on CT (arrow - image A) and bulges out from the right lacrimal fossa, to displace the right superior rectus muscle medially. It appears as a lobulated, heterogeneous high signal intensity lesion on T2 sequences (images B and D) and is isointense to muscle on T1 (image E). Avid enhancement followed contrast administration (images C and F). The diagnosis was confirmed histologically.

(Protocol: Image A: Siemens Definition AS 128 Slice CT , at 36mA and 120kV, 2mm slice thickness, Omnipaque 300 - 70mls i.v. Images B - F: MAGNETOM Symphony TIM 1.5T MRI. Image B: Axial T2, TR/TE - 4550/97ms , 5mm slice thickness, 448 x 306 matrix, non-contrast. Image C: Axial T1, TR/TE - 699/17ms , 3mm slice thickness, 320 x 240 matrix, Gadavist: 0.1 mmol/kg. Image D: Coronal T2, TR/TE - 4000/85ms , 3mm slice thickness, 384 x 288 matrix, non-contrast. Image E: Coronal T1, TR/TE - 792/14ms , 3mm slice thickness, 320 x 240 matrix, non-contrast. Image F: Coronal T1, TR/TE - 792/17ms , 3mm slice thickness, 320 x 240 matrix, Gadavist: 0.1 mmol/kg.)



Figure 16: Incidental CT finding of a lacrimal gland cyst (dacryops) in a 49 year old male seen as a cystic lesion arising from the palpebral lobe of the right lacrimal gland. The patient experienced swelling of the lateral aspect of his right eyelid, which fluctuated in size. The mean density measured with the placement of a ROI was 11.2HU in keeping with fluid. Diagnosis was confirmed after ophthalmic examination.

(Protocol: Siemens Definition AS 128 Slice CT , at 99mA and 120kV, 1mm slice thickness, non contrast).

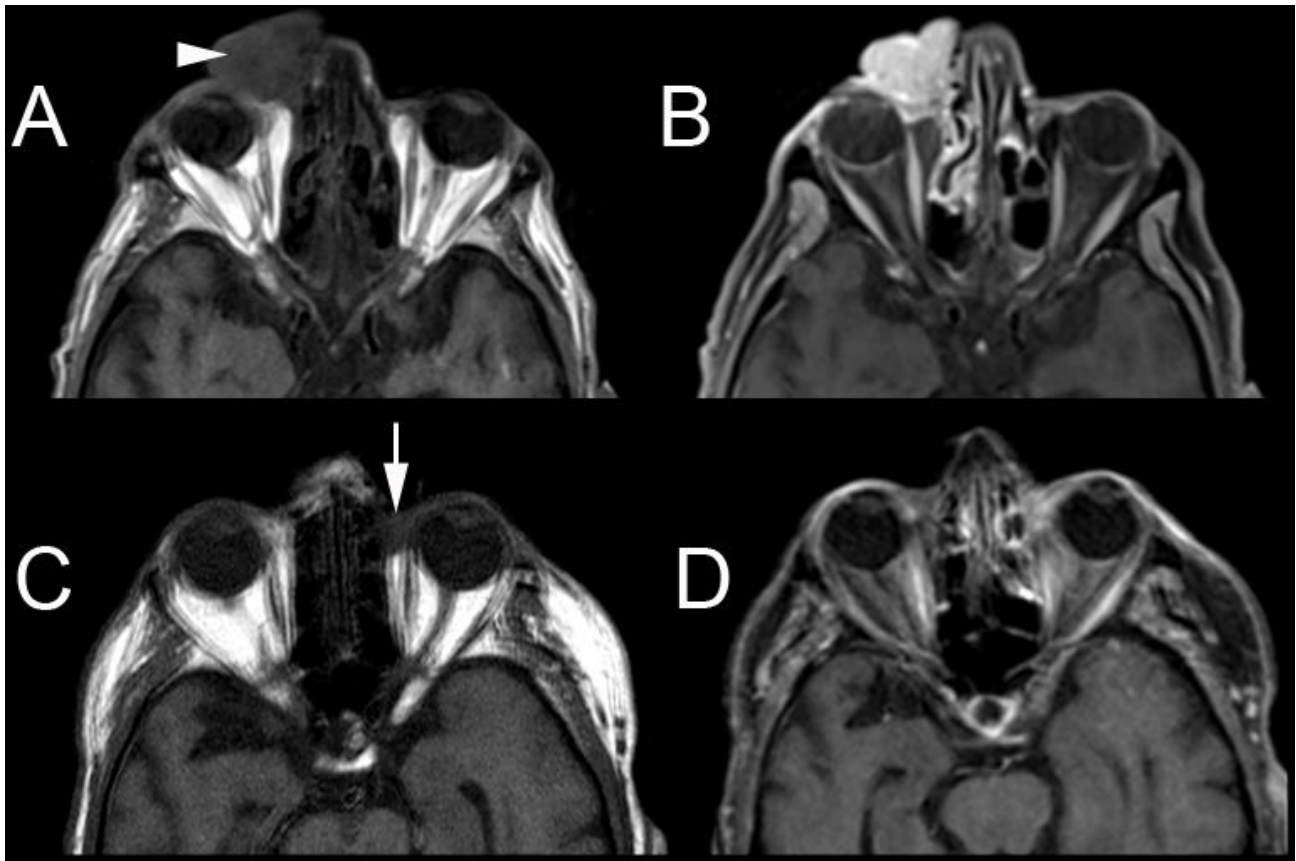


Figure 17: Biopsy proven basal cell carcinomas of the medial canthus in a 69 year old male (images A and B) and an 81 year old male patient (images C and D). Imaging in both cases was performed for staging and operative planning. Extensive exophytic growth (arrowhead) of the tumour is seen on images A and B (arrowhead). The tumour extends into the post septal space along the medial wall of the right orbit and demonstrates marked contrast enhancement. Less extensive involvement of the left medial canthus (arrow) is seen in the second patient (images C and D). Similar imaging characteristics are demonstrated.

(Protocol: Images A & B: Siemens MAGNETOM Avanto 1.5T. Image A: Axial T1, TR/TE - 500/8ms, 3.5mm slice thickness, 256 x 224 matrix, non-contrast. Image B: Axial T1, TR/TE - 645/11ms, 3.5mm slice thickness, 256 x 209 matrix, Gadavist: 0.1 mmol/kg. Images C & D: MAGNETOM Symphony TIM 1.5T MRI. Image C: Axial T1, TR/TE - 500/14ms, 3mm slice thickness, 256 x 192 matrix, non contrast. Image D: Axial T1, TR/TE - 639/12ms, 3mm slice thickness, 256 x 192 matrix, Gadavist: 0.1 mmol/kg.)

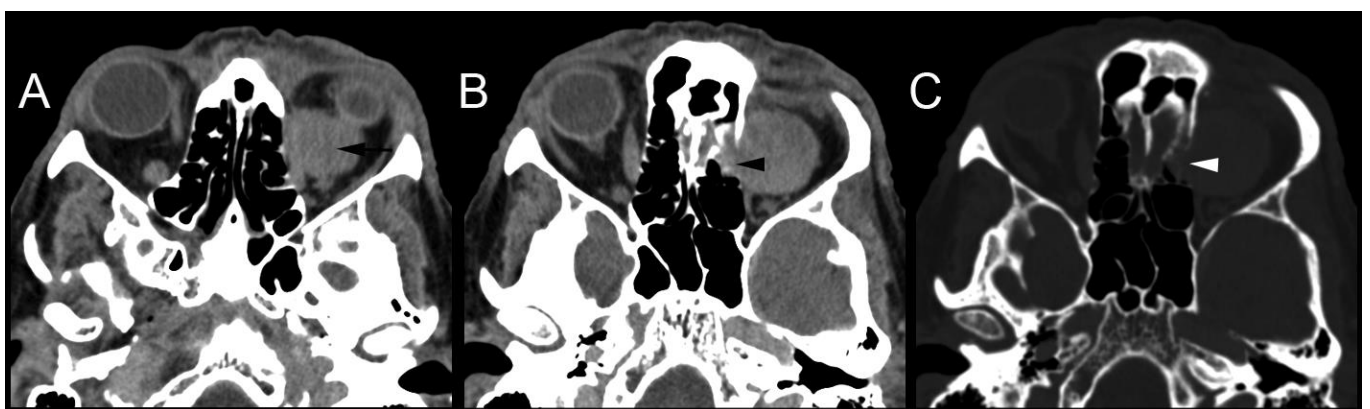


Figure 18: Axial CT images of an 82 year old man with orbital renal cell carcinoma metastasis. The patient complained of increasing left orbital pain and proptosis. A soft tissue density mass (arrow - image A) is seen in the left orbital apex, which displaces the globe anteriorly. It causes adjacent bone erosion (arrowheads - images B and C) and extends medially to invade the ethmoid air cells.

(Protocol: Siemens Sensation 16 Slice CT, at 212mA and 120kV, 1mm slice thickness, non contrast).

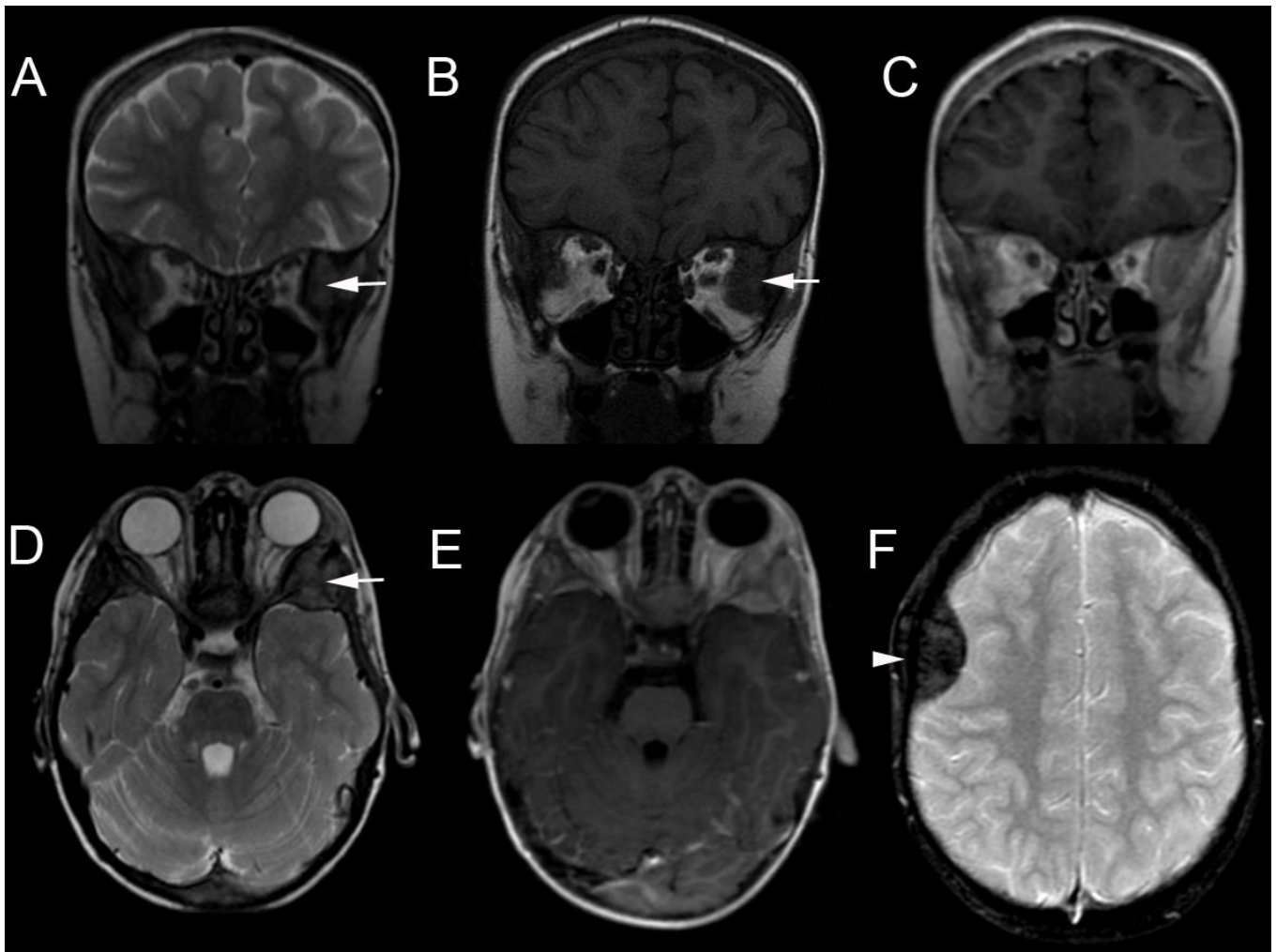


Figure 19: Coronal (images A to C) and axial (images D to F) MR images of a 5 year old child diagnosed with stage 4 neuroblastoma. An enhancing lesion is seen (arrows) within the left sphenoid wing which causes bony expansion and destruction. The lesion extends into the lateral aspect of the left orbit causing moderate exophthalmos due to mass effect. A second metastatic deposit with similar radiological appearances is seen in the right frontal calvarium. Findings are in keeping with neuroblastoma metastasis.

(Protocol: GE Signa EXCITE 1.5T MRI. Image A: Coronal T2, TR/TE - 4400/79ms , 3mm slice thickness, 256 x 224 matrix, non-contrast. Image B: Coronal T1, TR/TE - 420/12ms , 3mm slice thickness, 288 x 256 matrix, non-contrast. Image C: Coronal T1, TR/TE - 2377/9ms , 4mm slice thickness, 256 x 224 matrix, Gadavist: 0.1 mmol/kg. Image D: Axial T2, TR/TE - 4400/79ms , 3mm slice thickness, 256 x 224 matrix, non-contrast. Image E: Axial T1, TR/TE - 2347/9ms , 4mm slice thickness, 256 x 192 matrix, Gadavist: 0.1 mmol/kg. Image F: Axial T2, TR/TE - 320/224ms , 5mm slice thickness, 320 x 224 matrix, non-contrast.)

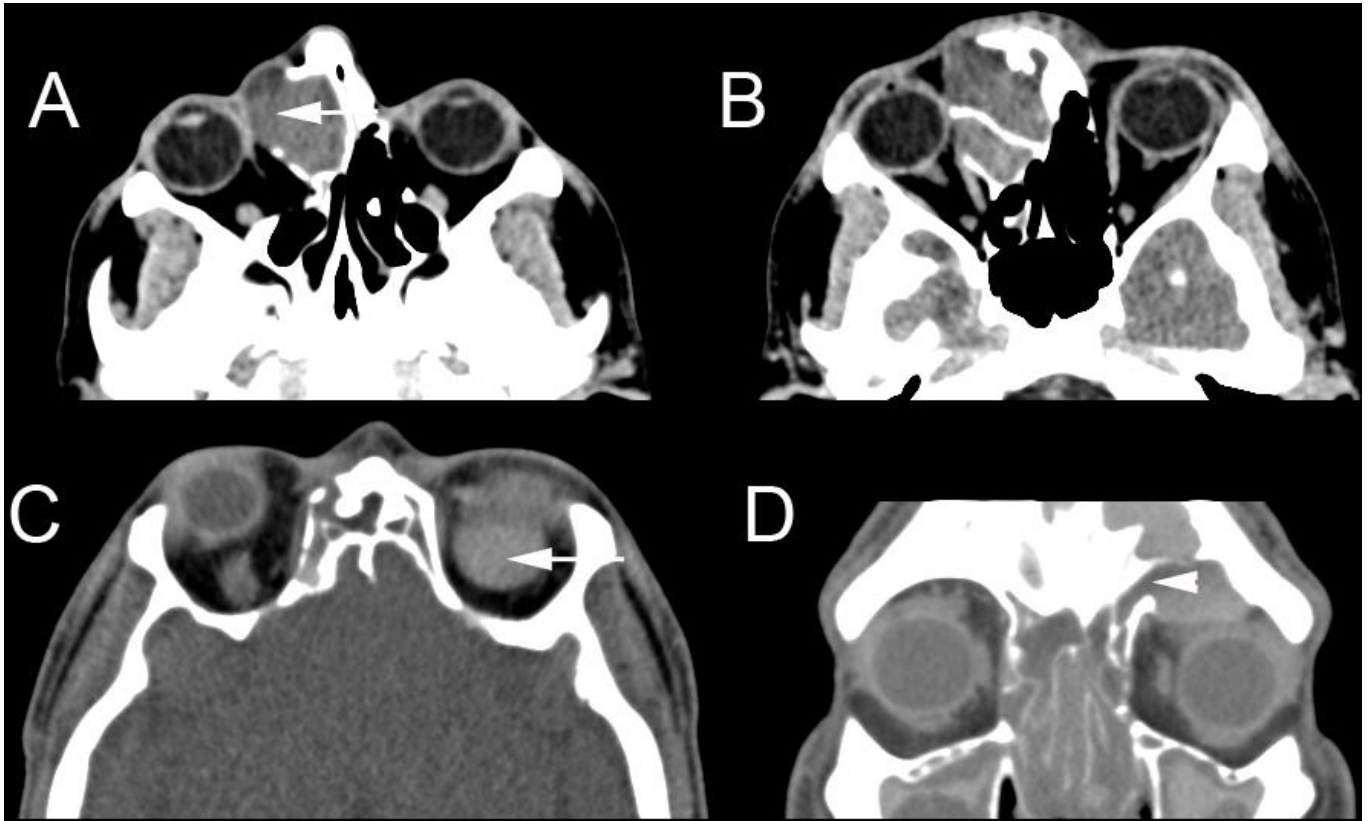


Figure 20: Ethmoid (images A and B) and frontal (images C and D) mucocoeles in a 25 year old and a 49 year old male patient respectively. Both patients had a history of chronic sinusitis. The anterior ethmoid air cells are expanded with inflammatory tissues and areas of complete bone resorption (arrow - image A) are evident. The visualized paranasal sinuses are completely opacified in the second patient. A superior left orbital lesion (arrow - image C) maintains direct communication with the left frontal sinus (arrowhead - image D). The imaging findings are characteristic of mucocoeles.

(Protocol: Images A & B: Siemens Definition AS 128 Slice CT, at 36mA and 120kV, 1mm slice thickness, non contrast. Images C & D: Philips Brilliance 16 slice CT, at 83mA and 120kV, 2mm slice thickness, non contrast).

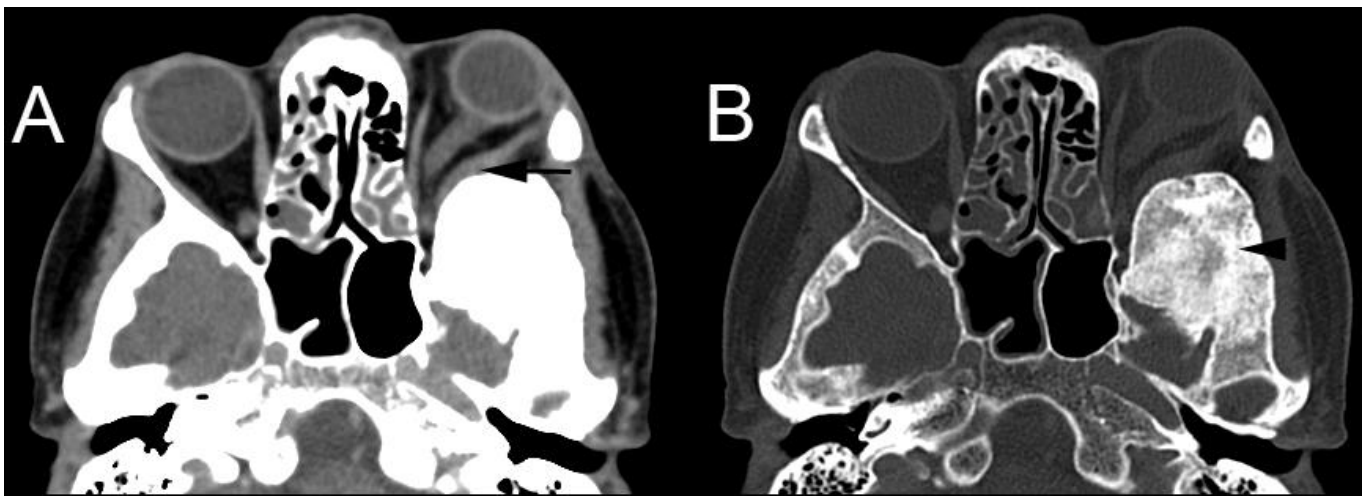


Figure 21: Fibrous dysplasia in a 64 year old female. Axial CT (images A and B) shows left exophthalmos secondary to bony expansion of the left sphenoid wing (arrow). A ground-glass pattern (arrowhead) characteristic of fibrous dysplasia is seen on bone window settings with no evidence of bone destruction. The rest of the base of skull bones are unaffected. Incidental note is made of bilateral opacified ethmoid air cells.

(Protocol: Siemens Sensation 16 Slice CT, at 310mA and 120kV, 4.5mm slice thickness, Omnipaque 300 - 70mls i.v.).

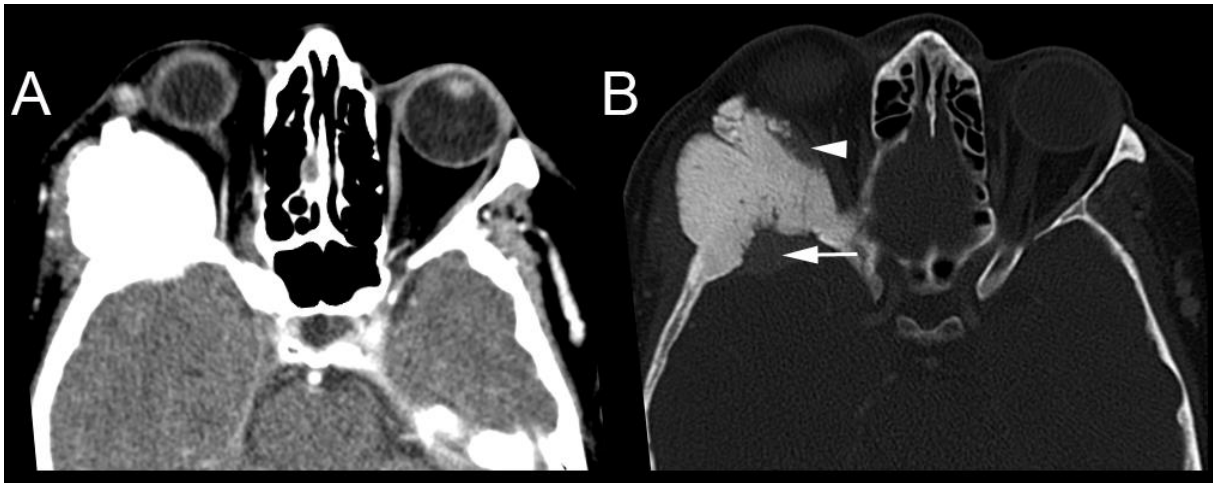


Figure 22: Right sphenoid wing meningioma in a 58 year old female patient who presented with deteriorating vision and proptosis. The meningioma resides in the anterior aspect of the middle cranial fossa and enhances avidly and homogeneously after contrast administration (arrow - image B). There is extensive reactive hyperostosis of the adjacent right sphenoid wing involving the lateral orbital wall (arrowhead).

(Protocol: Siemens Emotion 6 slice CT, at 160mA and 130kV, 3mm slice thickness, Omnipaque 300 - 60mls i.v.).

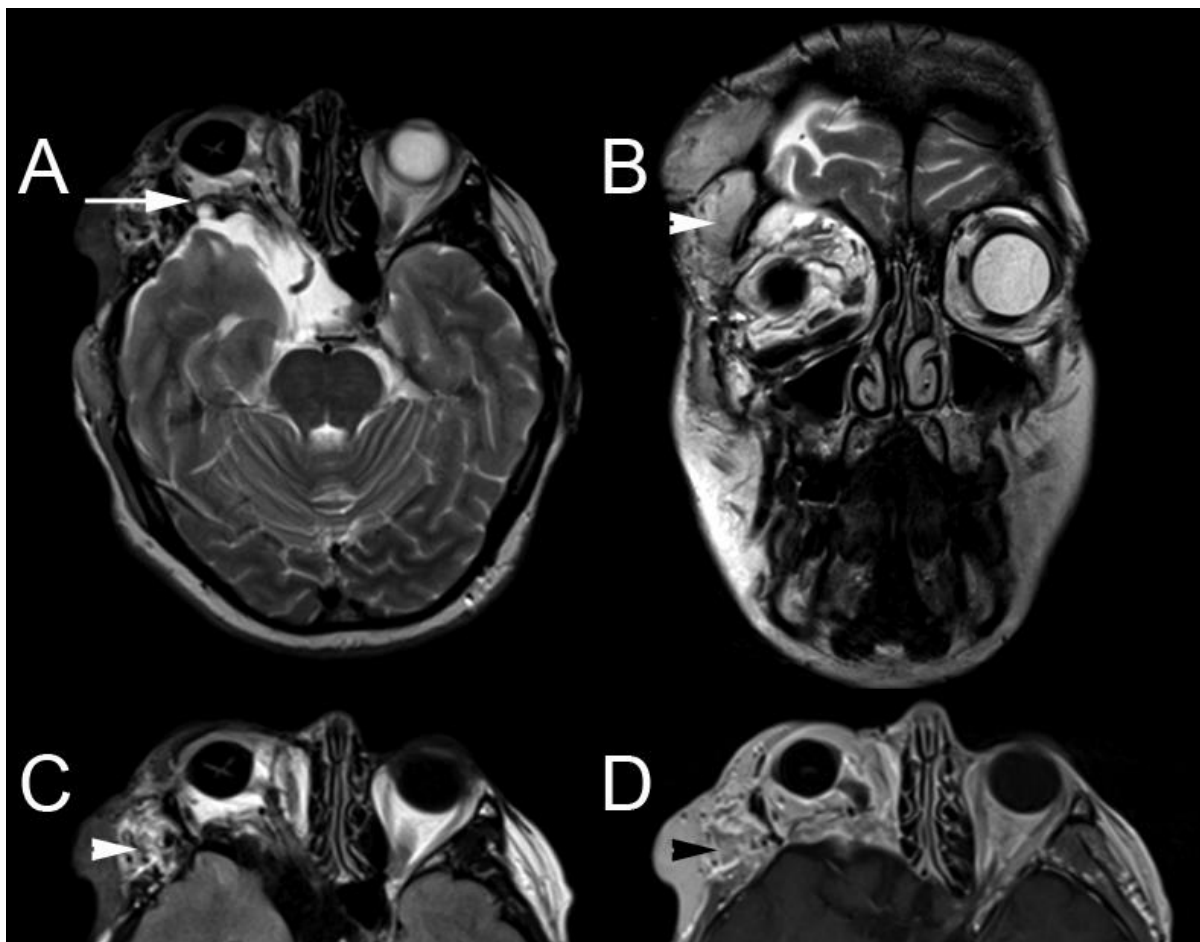


Figure 23: 42 year old female with a family history of neurofibromatosis type 1. The patient had previous enucleation for optic nerve glioma and an ocular prosthesis is noted within the right orbit. There is severe dysplasia of the right sphenoid bone (arrow - image A) resulting in marked bony deformity of the right orbit. A plexiform neurofibroma (arrowheads - images B to D) is noted over the right fronto-temporal region, which enhances markedly after contrast administration. The constellation of imaging findings is pathognomonic of neurofibromatosis type 1.

(Protocol: Siemens MAGNETOM Avanto 1.5T. Image A: Axial T2, TR/TE - 3620/98ms, 5mm slice thickness, 320 x 320 matrix, non-contrast. Image B: Coronal T2, TR/TE - 4000/102ms, 3.5mm slice thickness, 448 x 355 matrix, non-contrast. Image C: Axial FLAIR, TR/TE - 8000/98ms, 5mm slice thickness, 320 x 256 matrix, non-contrast. Image D: Axial T1, TR/TE - 500/11ms, 3.5mm slice thickness, 256 x 209 matrix, Gadavist: 0.1 mmol/kg.)

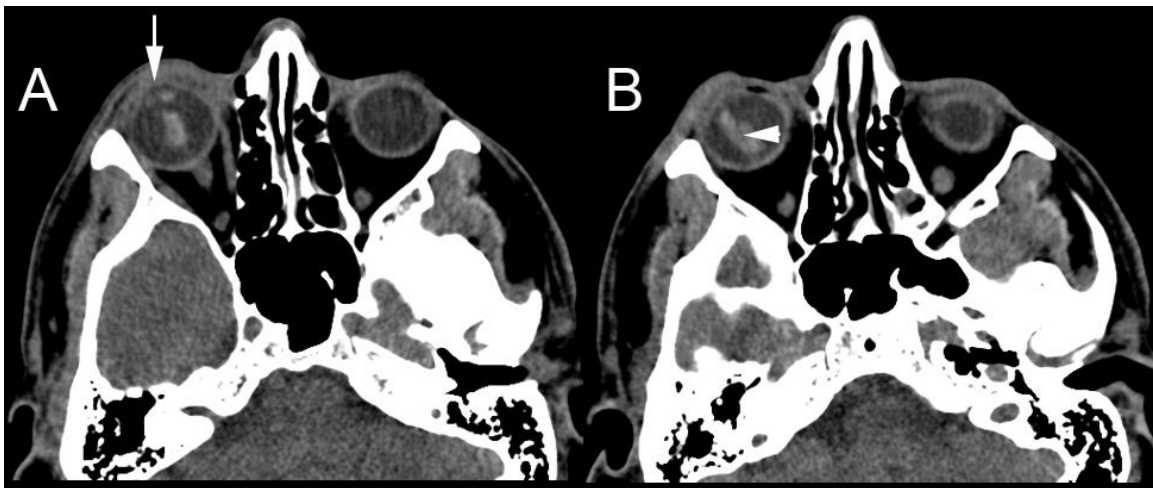


Figure 24: Intraocular penetration by a wire fence in a 38 year old male. The loose end of the wire traversed the anterior chamber, penetrated the lens (arrow - image A), and caused a linear vitreous hemorrhage along its path (arrowhead - image B). The globe contour is maintained and traumatic pre-septal soft tissue swelling is noted. (Protocol: Siemens Sensation 16 Slice CT, at 187mA and 120kV, 1mm slice thickness, non contrast).

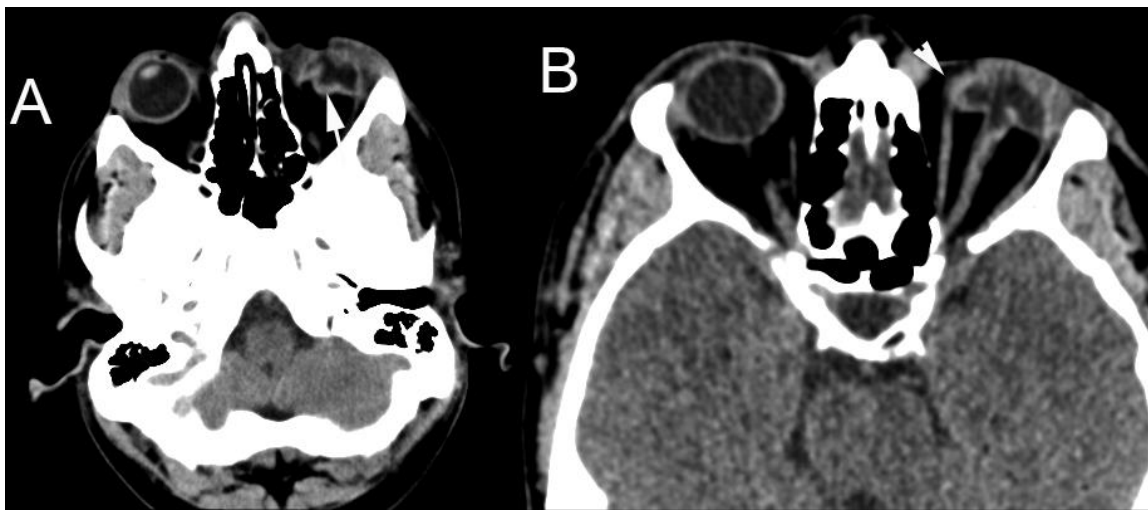


Figure 25: Traumatic globe rupture in a 29 year old male patient. CT shows collapse of the left globe with a characteristic 'flat tyre' appearance. There is no evidence of intra-ocular air or foreign body. Typical thickening of the posterior sclera is seen (arrow - image A) and the left globe has a hazy outline (arrowhead - image B). (Protocol: Siemens Definition AS 128 Slice CT, at 193mA and 120kV, 5mm slice thickness, non contrast).

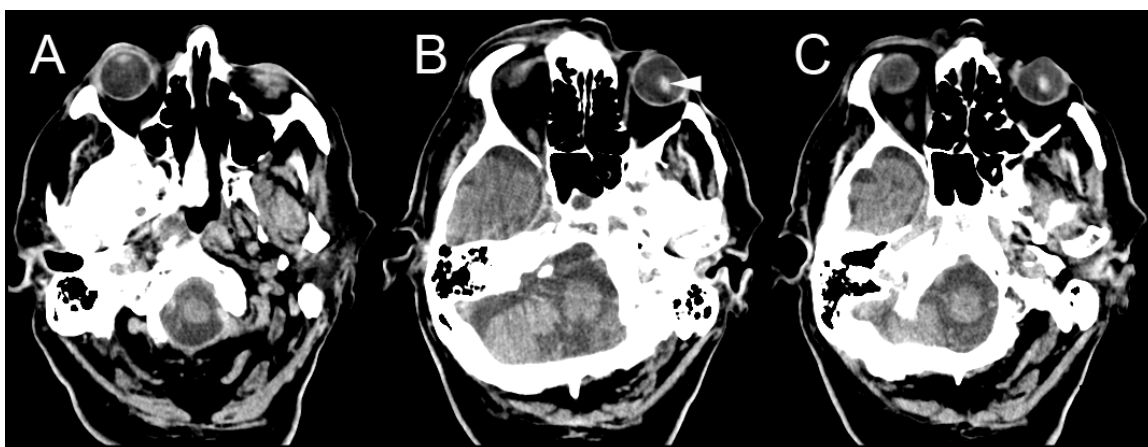


Figure 26: Traumatic dislocation of the lens in a 77 year old male passenger involved in a road traffic accident. Axial CT images demonstrate the left lens to be floating within the vitreous humor (arrowhead - images B and C). The globe contour is preserved and there were no external features of ocular injury. The diagnosis of traumatic dislocation of the lens was confirmed on ophthalmic examination. The uninjured right globe is shown for comparison (image A). (Protocol: GE HiSpeed CT Dual, at 95mA and 120kV, 4mm slice thickness, non contrast).

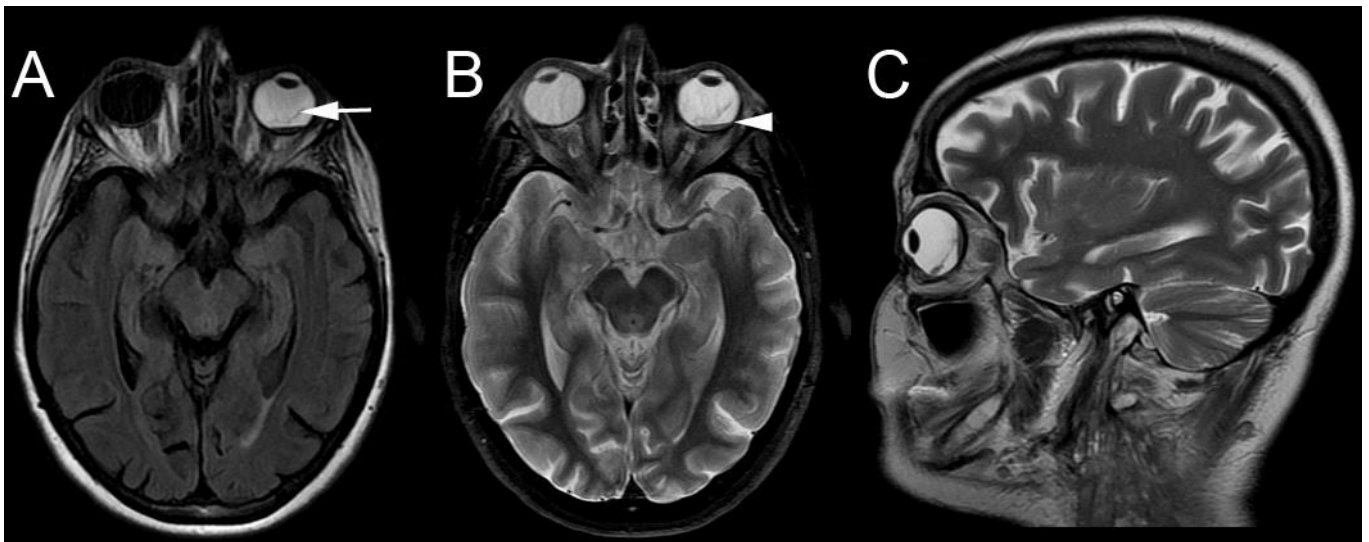


Figure 27: Rhegmatogenous retinal detachment in a 49 year old female who presented with deteriorating vision after injury in contact sports. The intraocular contents appear hyperintense on FLAIR (image A) in keeping with an extensive vitreous hemorrhage. The leading edge of an associated retinal detachment (arrow) is seen as a linear hypointensity within the left posterior chamber. A fluid- fluid level is seen in the sub-retinal space (arrowhead - image B) and represents layering of blood products. A tiny retinal tear (diagnosed on ophthalmic examination) allows vitreous fluid to seep through it and accumulate in the potential space between the neurosensory retina and the underlying retinal pigment epithelium. Clinical and imaging findings support a diagnosis of rhegmatogenous retinal detachment secondary to traumatic vitreo-retinal traction.

(Protocol: GE Signa EXCITE 1.5T MRI. Image A: Axial FLAIR, TR/TE - 8502/162ms , 6mm slice thickness, 320 x 224 matrix, non-contrast. Image B: Axial T2, TR/TE - 512/256ms , 6mm slice thickness, 512 x 256 matrix, non-contrast. Image C: Sagittal T2, TR/TE - 5000/94ms , 5mm slice thickness, 384 x 256 matrix, non-contrast.)



Figure 28: Blow-out fracture in a 29 year old woman. A 'teardrop' sign (arrow - image A) is seen on the frontal radiograph acquired after facial trauma and represents orbital fat herniation through the orbital floor defect. This right inferior orbital margin appears intact, and the density projecting over the superior aspect of the right maxillary sinus represents intraocular fat herniation through an orbital floor fracture. Axial CT in bone window settings (image B) confirms a right orbital floor fracture and the presence of air bubbles (arrowhead) in the orbit due to communication with the underlying sinus. The inferior rectus muscle (arrowhead - image C) was not entrapped in the fracture, and retro-orbital fat herniation (arrow) is again seen on this coronal reconstruction. The imaging findings are in keeping with a 'blow-out' fracture of the right orbit.

(Protocol: Images B & C: GE HiSpeed CT Dual, at 95mA and 120kV, 4mm slice thickness, non contrast).



Figure 29: Orbital foreign bodies in three different patients. Streak artifact caused by a metallic foreign body (arrow - image A) in the retro-bulbar space in a patient with a history of pellet injury to the left orbit. A superficial foreign body is seen at the corneo-scleral junction (arrowhead - image B) of a patient who had sustained a welding injury. Image C shows an intra-ocular pellet. The right lens is slightly deformed but the globe maintains its contour and there is no evidence of an associated vitreous hemorrhage.

(Protocol: Image A: Siemens Sensation 16 Slice CT, at 193mA and 120kV, 1mm slice thickness, non contrast. Image B: Siemens Sensation 16 Slice CT, at 233mA and 120kV, 1mm slice thickness, non contrast. Image C: Siemens Definition AS 128 Slice CT, at 99mA and 120kV, 1mm slice thickness, non contrast).

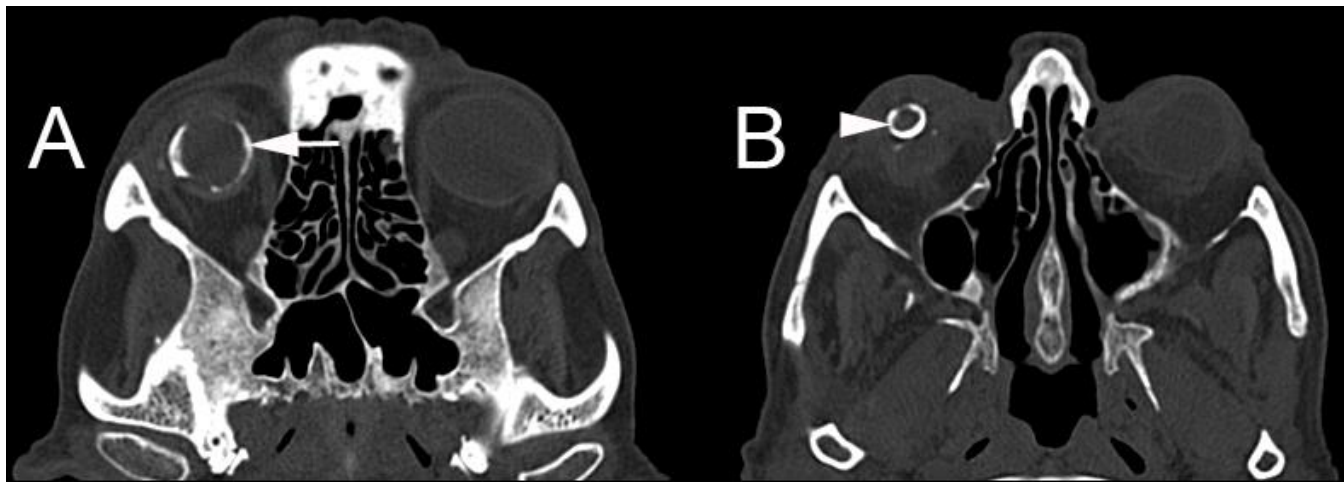


Figure 30: Phthisis bulbi in a 45 year old blind male patient with previous ocular trauma. Axial CT in bone algorithm (images A and B) demonstrate a shrunken right (microphthalmia) and dense sclero-choroidal calcifications in keeping with phthisis bulbi.

(Protocol: Siemens Sensation 16 Slice CT, at 150mA and 120kV, 1mm slice thickness, non contrast).

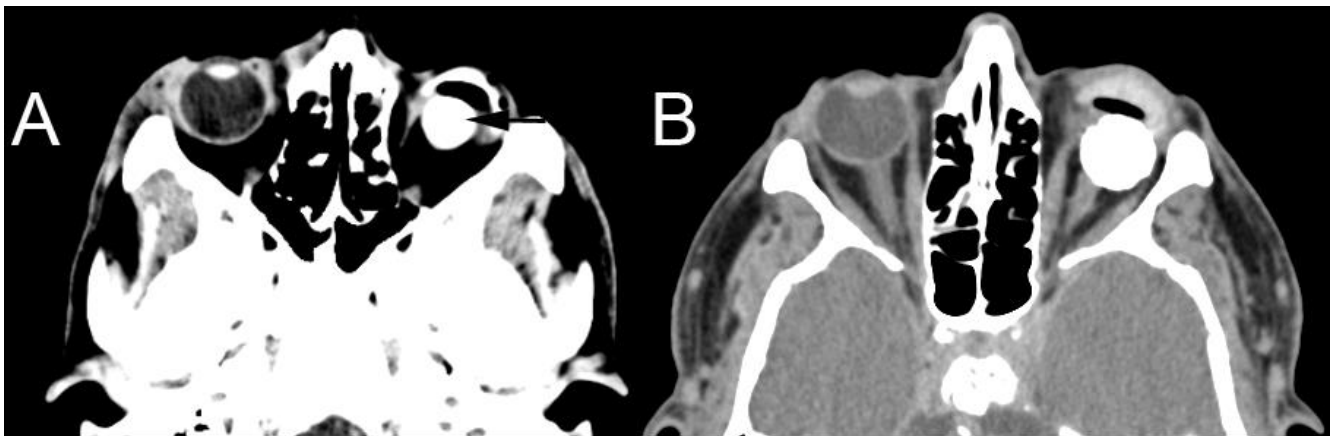


Figure 31: Non-contrast CT scan through the orbits demonstrates a prosthetic left eye (arrow - image A) in a 25 year old man. The prosthesis is seen as a high density rounded structure replacing the left globe. Enucleation removes the globe leaving the extra-ocular muscles and remaining orbital contents intact (image B).

(Protocol: Siemens Sensation 16 Slice CT, at 310mA and 120kV, 4.5mm slice thickness, non contrast).

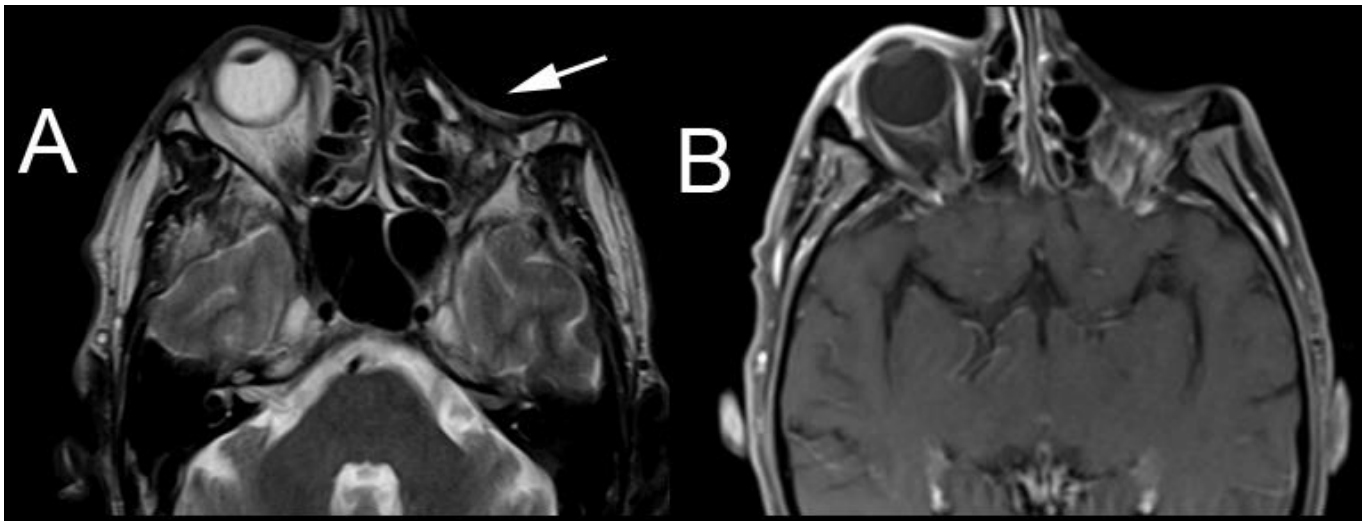


Figure 32: Axial T2 and contrast enhanced T1 MR (images A and B respectively) in a 55 year old man previously treated with orbital exenteration for an invasive basal cell carcinoma. There is evidence of total left exenteration (arrow) with removal of all orbital contents including the periorbita and eyelids.

(Protocol: Siemens MAGNETOM Avanto 1.5T. Image A: Axial T2, TR/TE - 5000/89ms , 5mm slice thickness, 384 x 261 matrix, non-contrast. Image B: Axial T1, TR/TE - 500/11ms, 3.5mm slice thickness, 256 x 209 matrix, Gadavist: 0.1 mmol/kg).

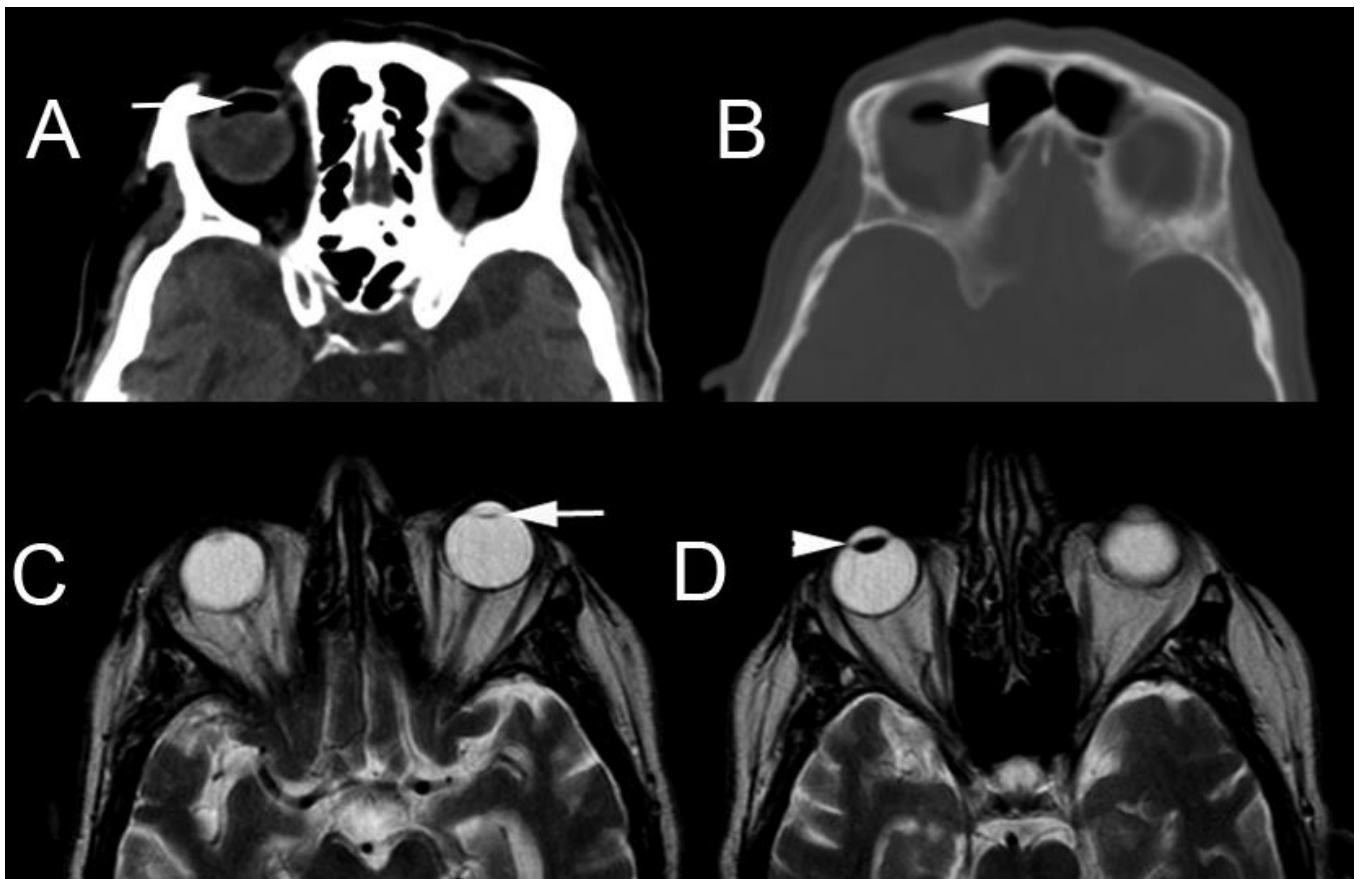


Figure 33: Axial non enhanced CT (images A and B) obtained in a 85 year old woman demonstrates air within the right anterior chamber (arrows) following cataract surgery. Axial T2 weighted MR in a second patient shows a left lens implant (arrows) for the treatment of cataracts (arrow - image C). The normal right lens (arrowhead - image D) is shown for comparison.

(Protocol: Images A & B: GE HiSpeed CT Dual, at 125mA and 120kV, 4mm slice thickness, non contrast.

Images C & D: GE Signa EXCITE 1.5T MRI. Axial T2, TR/TE - 4900/97ms , 5mm slice thickness, 384 x 256 matrix, non-contrast).

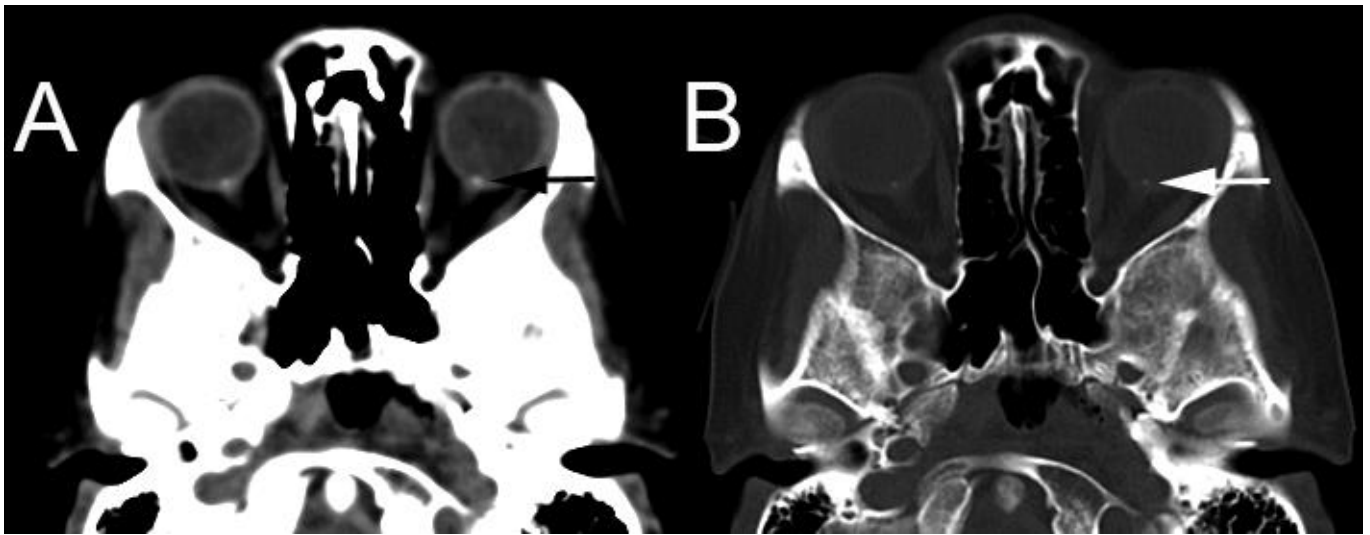


Figure 34: Non enhanced CT (images A and B) in a 45 year old female shows an incidental finding of bilateral small rounded calcifications on the optic disc surfaces (arrows) characteristic of optic nerve drusen.

(Protocol: Siemens Sensation 16 Slice CT, at 310mA and 120kV, 4.5mm slice thickness, non contrast).

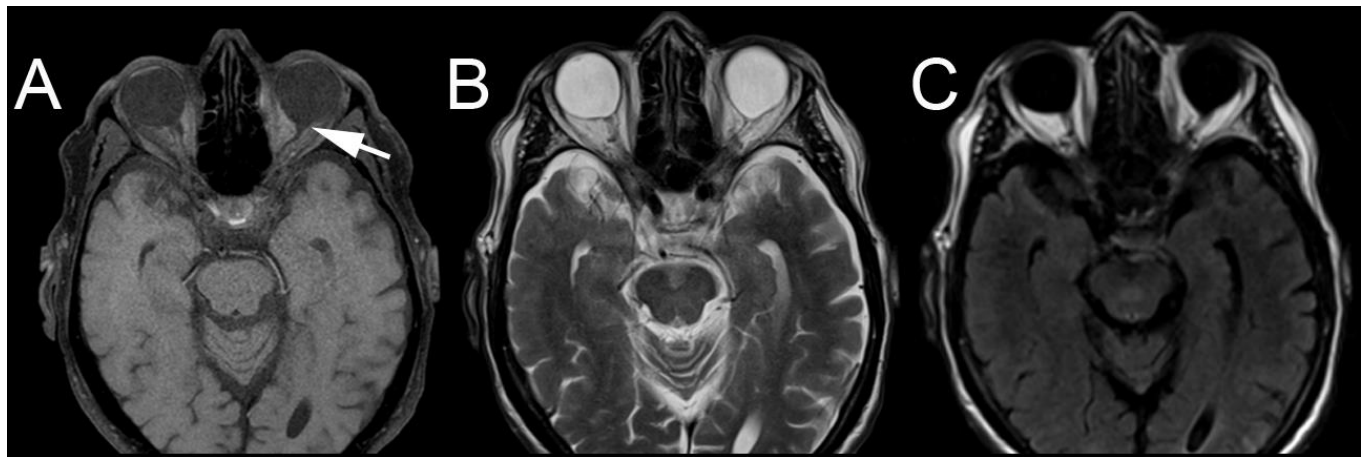


Figure 35: Bilateral optic disc colobomas in a 80 year old male patient. The optic nerve heads are displaced posteriorly and there is 'funnel-shaped' excavation (arrow - image A) of the posterior fundus. The sclera at the margin of the defect is thinned and everted.

(Protocol: Siemens Symphony 1.5T MRI. Image A: Axial T1, TR/TE - 699/17ms , 3mm slice thickness, 320 x 240 matrix, non-contrast. Image B: Axial T2, TR/TE - 4550/97ms , 5mm slice thickness, 448 x 306 matrix, non-contrast. Image C: Axial FLAIR, TR/TE - 9340/156ms , 5mm slice thickness, 256 x 204 matrix, non-contrast).

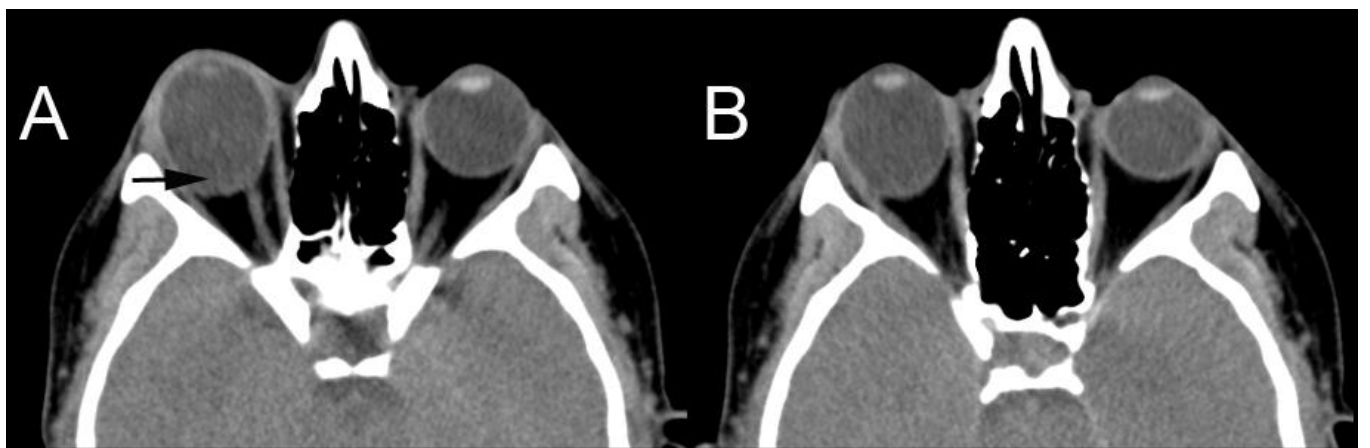


Figure 36: Staphyloma in a 34 year old female who presented with progressive myopia. Axial CT (images A and B) shows elongation of the right globe (along its axis) due to focal posterior deformity (arrow). No abnormal enhancement in the uveo-sclera was seen post contrast administration. The structural alterations of the globe are characteristic of posterior staphyloma.

(Protocol: Siemens Emotion 6 slice CT, at 60mA and 130kV, 3mm slice thickness, non contrast).

CATEGORY	CONDITIONS
Vascular	<ul style="list-style-type: none"> • Capillary Hemangioma • Orbital Varix • Arterio-venous malformation • Carotico-cavernous fistula
Inflammatory & Infectious	<ul style="list-style-type: none"> • Infection • Ocular tuberculoma • Orbital pseudotumour • Optic neuritis
Endocrine	<ul style="list-style-type: none"> • Thyroid orbitopathy • Hyperparathyroidism
Neoplastic	<ul style="list-style-type: none"> • Choroidal melanoma • Ocular metastasis • Optic glioma • Pilocytic astrocytoma • Optic nerve sheath meningioma • Lymphoma • Lacrimal gland neoplasms • Basal and squamous cell carcinomas
Paranasal sinuses	<ul style="list-style-type: none"> • Cellulitis • Mucocele • Inverted papilloma
Osseous	<ul style="list-style-type: none"> • Fibrous dysplasia • Hyperostosis (associated with meningioma) • Neurofibromatosis type-1
Trauma	<ul style="list-style-type: none"> • Penetrating injuries • Non-penetrating injuries
Iatrogenic / Congenital	<ul style="list-style-type: none"> • Implants • Exenteration • Cataract surgery • Optic disc Drusen • Coloboma • Staphyloma

Table 1: Etiological categories of adult ocular and orbital pathology

		Modality			
Case #	Diagnosis	Radiography	US	CT	MRI
A. VASCULAR					
1	Capillary hemangioma	Large lesions may cause remodelling of the orbit.	Circumscribed lesion with moderate to high echogenicity. No flow on doppler scanning.	Lacks a capsule therefore appears as a lobulated, irregularly marginated mass. Crosses tissue planes.	Often T1 isointense and moderately T2 hyperintense. (Appearances may however vary according to phase). Thin dark fibrous septa, and flow voids are characteristic.
2	Orbital varix	Calcified phleboliths are characteristic.	Tortuous anechoic tubular channels with low-velocity Doppler flow.	Intrinsically hyperdense on CT. Enhance profusely with contrast.	Prominent flow voids on MRI. Characteristically lack internal septations.
3	Arteriovenous malformation (AVM)		Abnormal cluster of vessels, and engorged ophthalmic veins.	Engorged ophthalmic veins. Intracranial AVMs may invade the orbit directly.	Engorged ophthalmic veins. Intracranial AVMs may invade the orbit directly.
4	Carotico-cavernous fistula (CCF)		Engorged superior ophthalmic vein. Arterialised veins may be seen on Doppler ultrasound.	Distended ipsilateral superior ophthalmic vein and engorgement of the ipsilateral cavernous sinus.	Distended ipsilateral superior ophthalmic vein and engorgement of the ipsilateral cavernous sinus.
B. INFLAMMATORY & INFECTIOUS					
5	Orbital cellulitis		Demonstrates soft tissue oedema and swelling.	Diffuse soft tissue swelling, orbital fat stranding and small pockets of gas. Abscess formation may complicate the condition.	Diffuse soft tissue swelling, orbital fat stranding and small pockets of gas. Abscess formation may complicate the condition.
6	Choroidal tuberculoma		Presents as a choroidal mass. Retinal detachment may complicate the condition.	Appears as a choroidal mass and mimics ocular lymphoma and choroidal melanoma.	Appears as a choroidal mass and mimics ocular lymphoma and choroidal melanoma. Retinal detachment may complicate the condition.
7	Orbital pseudotumour		May mimic several orbital disorders and pseudotumour remains a diagnosis of exclusion.	Often presents as a diffuse infiltrative mass. Radiological appearance may mimic several orbital disorders and pseudotumour remains a diagnosis of exclusion.	Often presents as a diffuse infiltrative mass. Radiological appearance may mimic several orbital disorders and pseudotumour remains a diagnosis of exclusion.
8	Optic neuritis				Diffuse swelling of the optic nerve with focal plaques of T2 hyperintensity. Occasional contrast enhancement is seen.
C. ENDOCRINE					
9	Thyroid orbitopathy			Muscular involvement is often bilateral and symmetrical and typically spares the muscle tendons. Orbital fat is initially spared.	Muscular involvement is often bilateral and symmetrical and typically spares the muscle tendons. Orbital fat is initially spared.
10	Hyper-parathyroidism			Characteristic coarse calcifications typically seen at the corneo-scleral junction.	Characteristic coarse calcifications typically seen at the corneo-scleral junction.

Table 2 (a): Imaging findings in ocular and orbital pathology (vascular, inflammatory, infectious & endocrine)

		Modality		
Case #	Diagnosis	Radiography	CT	MRI
D. NEOPLASTIC				
11	Choroidal melanoma	Plaque like or discoid solid lesion, of low to medium echogenicity. Often demonstrates a 'collar button shape'. Internal vascularity is often demonstrated on Doppler studies.	Intrinsically hyperdense on CT. Moderate contrast enhancement is often appreciated.	High T1 signal intensity and low T2 signal intensity (due to presence of melanin).
12	Optic nerve glioma	Widening of the optic canal may be seen.	Tubular or fusiform enlargement of the optic nerve is seen and 'kinking' of the nerve is characteristic. Enhancement is variable.	Tubular or fusiform enlargement of the optic nerve is seen and 'kinking' of the nerve is characteristic. Enhancement is variable.
13	Optic nerve sheath meningioma		Appears hyperdense with psammomatous calcifications in up to 50%. 'Tram-track' enhancement along the sheath is characteristic.	Fusiform enlargement of the optic nerve sheath. 'Tram-track' enhancement along the sheath is characteristic.
14	Lymphoma		Appears hyperdense. Avid enhancement occurs in the post contrast sequences.	Low signal intensity on both T1 and T2 sequences. Avid enhancement occurs in the post contrast sequences. Characteristically crosses the compartmental boundaries.
15	Adenoid cystic carcinoma (lacrimal gland)		Irregularly marginated neoplasm which may cause erosion of the adjacent bone.	Displays a heterogeneous signal, with moderate to strong contrast enhancement.
16	Lacrimal gland cyst		Well defined cyst related to the lacrimal gland, containing fluid with water density.	Well defined cyst related to the lacrimal gland, containing fluid which follows the signal intensity of water.
17	Basal cell carcinoma		Cutaneous lesions, with variable invasion and contrast enhancement.	Cutaneous lesions, with variable invasion and contrast enhancement.
18	Renal cell metastasis		Secondary deposits may involve the globe, orbit and intracranial compartments.	Secondary deposits may involve the globe, orbit and intracranial compartments.
19	Neuroblastoma metastasis		Secondary deposits may involve the globe, orbit and intracranial compartments.	Secondary deposits may involve the globe, orbit and intracranial compartments.

Table 2 (b): Imaging findings in ocular and orbital pathology (neoplastic)

		Modality		
Case #	Diagnosis	Radiography	CT	MRI
E. PARANASAL SINUS PATHOLOGY				
20	Mucocoele	May demonstrate opacification and expansion of the affected paranasal sinus.	Complete opacification of the affected sinus, with expanded, thinned margins. The lesion may extend through a bony defect into the extraconal compartment. Only peripheral enhancement (if any) is seen.	Signal intensity varies according to the proportions of water, protein and mucus. Presents as an extraconal lesion. Only peripheral enhancement (if any) is seen.
F. OSSEOUS				
21	Fibrous dysplasia	Smooth expansion of the affected bone.	Bone expansion with a characteristic ground glass matrix resulting in deformity of the orbital cone.	Extra-conal lesion which often presents with unilateral exophthalmos.
22	Meningioma (sphenoid wing)		Hyperdense soft tissue lesion with avid enhancement and adjacent hyperostosis. May contain calcifications.	Soft tissue lesion with avid enhancement and adjacent hyperostosis. Calcifications appear as signal voids.
23	Neuro fibromatosis type-1	Dysplasia of the greater wing of the sphenoid results in orbital deformity.	Dysplasia of the greater wing of the sphenoid results in orbital deformity.	Dysplasia of the greater wing of the sphenoid results in orbital deformity.

Table 2 (c): Imaging findings in ocular and orbital pathology (paranasal sinus & osseous pathology)

		Modality			
Case #	Diagnosis	Radiography	US	CT	MRI
F. TRAUMATIC					
24	Intraocular penetration	Appearances depend on the mechanism of injury and the compartments involved.		Appearances depend on the mechanism of injury and the compartments involved.	Appearances depend on the mechanism of injury and the compartments involved.
25	Globe rupture			Characteristic 'flat tire' appearance. Thickening of the posterior sclera with a hazy outline of the globe.	Characteristic 'flat tire' appearance. Thickening of the posterior sclera with a hazy outline of the globe.
26	Lens dislocation			Dislocated lens seen floating within the vitreous humour. Globe contour is preserved.	Dislocated lens seen floating within the vitreous humour. Globe contour is preserved.
27	Retinal detachment		Appears as a smooth, bright and folded membrane in the vitreous humour, which is reflective and freely moving on real time ultrasound imaging.		Leading edge of the retinal detachment seen as a linear hypointensity. Haemorrhage is seen in the posterior chamber and sub-retinal space, where layering of blood products may occur.
28	Blow-out fracture	'Teardrop' sign on the frontal radiograph. The inferior orbital margin remains intact.		Orbital floor fracture with presence of air bubbles in the orbit due to communication with the underlying maxillary sinus. Entrapment of the inferior rectus muscle in the fracture may occur.	Orbital fat herniation, soft tissue oedema and entrapment of the inferior rectus muscle may be seen.
29	Foreign bodies	Orbital radio-opaque foreign bodies can be detected.	Appearances depend on the type of foreign body and the orbital compartment involved.	Appearances depend on the type of foreign body and the orbital compartment involved.	Appearances depend on the type of foreign body and the orbital compartment involved.
30	Phthisis bulbi	Disorganised globe. Curvilinear choroido-scleral calcifications and clumps of dystrophic calcifications within the vitreous humour may be seen as hyperechoic foci.		Curvilinear choroido-scleral calcifications and clumps of dystrophic calcifications within the vitreous humour may be seen.	Atrophic scarred globe. Calcifications appear as signal voids.

Table 2 (d): Imaging findings in ocular and orbital pathology (traumatic)

		Modality			
Case #	Diagnosis	Radiography	US	CT	MRI
G. IATROGENIC / CONGENITAL					
31	Prosthesis	Appearances depend on the type of prosthesis.		Appearances depend on the type of prosthesis.	Appearances depend on the type of prosthesis.
32	Exenteration			Iatrogenic removal of all orbital contents including the periorbita and eyelids (as opposed to <i>enucleation</i> which removes the globe while leaving the extra-ocular muscles and remaining orbital contents intact).	Iatrogenic removal of all orbital contents including the periorbita and eyelids (as opposed to <i>enucleation</i> which removes the globe while leaving the extra-ocular muscles and remaining orbital contents intact).
33	Post-cataract surgery			Lens implant. A small amount of air may be seen in the anterior chamber.	Lens implant. A small amount of air may be seen in the anterior chamber.
34	Optic nerve Drusen		Echogenic foci on or within the optic nerve head. Posterior acoustic shadowing is seen with larger lesions.	Small rounded calcifications on the optic disc surfaces.	
35	Optic disc coloboma			The optic nerve head is displaced posteriorly and there is 'funnel-shaped' excavation of the posterior fundus	The optic nerve head is displaced posteriorly and there is 'funnel-shaped' excavation of the posterior fundus. The sclera at the margin of the defect is thinned and everted.
36	Staphyloma			Elongation of the globe (along its axis) due to focal posterior deformity.	Elongation of the globe (along its axis) due to focal posterior deformity. No abnormal enhancement is seen.

Table 2 (e): Imaging findings in ocular and orbital pathology (iatrogenic & congenital)

ABBREVIATIONS

AVM = arteriovenous malformation
 CCF = carotico-cavernous fistula
 CT = computed tomography
 MR = magnetic resonance
 US = ultrasound

KEYWORDS

Orbit; globe; adult; pathology; vascular; inflammatory; infectious; endocrine; neoplastic; paranasal sinuses; bone lesions; trauma; iatrogenic

Online access

This publication is online available at:
www.radiologycases.com/index.php/radiologycases/article/view/1525

Peer discussion

Discuss this manuscript in our protected discussion forum at:
www.radiopolis.com/forums/JRCR

Interactivity

This publication is available as an interactive article with scroll, window/level, magnify and more features.
 Available online at www.RadiologyCases.com

Published by EduRad



www.EduRad.org